Nuclear Science and Techniques (2024) 35:215
https://doi.org/10.1007/s41365-024-01585-0

Progress in ab initio in-medium similarity renormalization group and coupled-channel method with coupling to the continuum

Xin-Yu Xu[1] · Si-Qin Fan[1] · Qi Yuan[1,2] · Bai-Shan Hu[3,4] · Jian-Guo Li[2,5] · Si-Min Wang[6,7] · Fu-Rong Xu[1,2]

Received: 15 July 2024 / Revised: 14 August 2024 / Accepted: 31 August 2024

Abstract
Over the last decade, nuclear theory has made dramatic progress in few-body and ab initio many-body calculations. These great advances stem from chiral effective field theory (χEFT), which provides an efficient expansion and consistent treatment of nuclear forces as inputs of modern many-body calculations, among which the in-medium similarity renormalization group (IMSRG) and its variants play a vital role. On the other hand, significant efforts have been made to provide a unified description of the structure, decay, and reactions of the nuclei as open quantum systems. While a fully comprehensive and microscopic model has yet to be realized, substantial progress over recent decades has enhanced our understanding of open quantum systems around the dripline, which are often characterized by exotic structures and decay modes. To study these interesting phenomena, Gamow coupled-channel (GCC) method, in which the open quantum nature of few-body valence nucleons coupled to a deformed core, has been developed. This review focuses on the developments of the advanced IMSRG and GCC and their applications to nuclear structure and reactions.

Keywords Ab initio calculations · Chiral effective field theory · In-medium similarity renormalization group · Gamow coupled channel · Resonance and continuum · Open quantum systems

1 Introduction

In the past decades, great progress in nuclear forces [1, 2], and ab initio many-body theories [3–10] has been made. Using low-energy expansion with nucleons and pions as explicit degrees of freedom, the chiral effective field theory (χEFT) [1, 2] with Weinberg's power counting (WPC) [11–13] provides a powerful framework in which two- and many-nucleon interactions, and electroweak currents can be naturally derived with the uncertainties

---

Dedicated to Professor Wenqing Shen in honour of his 80th birthday.

This work was supported by the National Key R&D Program of China under Grant Nos. 2023YFA1606400 and 2022YFA1602303; the National Natural Science Foundation of China under Grants Nos. 12335007, 12035001, 11921006, 12347106, 12147101, and 12205340; the Gansu Natural Science Foundation under Grant No. 22JR5RA123; and the U.S. Department of Energy (DOE), Office of Science, under SciDAC-5 (NUCLEI collaboration).

✉ Si-Min Wang
wangsimin@fudan.edu.cn

✉ Fu-Rong Xu
frxu@pku.edu.cn

[1] School of Physics, and State Key Laboratory of Nuclear Physics and Technology, Peking University, Beijing 100871, China

[2] Southern Center for Nuclear-Science Theory (SCNT) Institute of Modern Physics, Chinese Academy of Sciences, Huizhou 516000, China

[3] National Center for Computational Sciences, Oak Ridge National Laboratory, Oak Ridge, TN 37831, USA

[4] Physics Division, Oak Ridge National Laboratory, Oak Ridge, TN 37831, USA

[5] Institute of Modern Physics, Chinese Academy of Sciences, Lanzhou 730000, China

[6] Institute of Modern Physics Key Laboratory of Nuclear Physics and Ion-beam Application (MOE), Fudan University, Shanghai 200433, China

[7] Shanghai Research Center for Theoretical Nuclear Physics, NSFC and Fudan University, Shanghai 200438, China

associated with each expansion order. The three-nucleon force (3NF) has been shown to be crucial in the quantitative predictions of nuclear structure [14–30].

However, it still challenges current calculations to extend the ab initio frontier to heavier nuclei. In ab initio calculations, one needs to handle the coupling between low and high momenta of nuclear forces. In recent years, new approaches to nuclear forces have been developed based on the ideas of the renormalization group (RG), whereby high-momentum degrees of freedom are decoupled by lowering the resolution (or cutoff) scale in nuclear forces to typical nuclear structure momentum scales, which greatly accelerates the convergence of the nuclear structure calculations [31–33]. The similarity renormalization group (SRG) [34, 35] provides a powerful method to decouple the high-momentum degrees of freedom, using continuous unitary transformations that suppress off-diagonal matrix elements and drive the Hamiltonian toward a band-diagonal form. The SRG softened nuclear forces can accelerate many-body calculations without compromising the nature of realistic nuclear forces or the accuracy of calculations.

The ab initio SRG method has been further developed to treat the nuclear many-body problems, which are in-medium similarity renormalization group (IMSRG) [36–38] for the ground states of closed-shell nuclei and valence-space IMSRG (VS-IMSRG) [21, 28, 39] for open-shell nuclei. The IMSRG employs a continuous unitary transformation of the many-body Hamiltonian to decouple the ground state from all excitations, thereby solving the many-body problems [10, 21, 28, 37, 39, 40]. Other advanced ab initio many-body methods include coupled-cluster (CC) theory [41–43], many-body perturbation theory (MBPT) [6, 44, 45], and self-consistent Green's function (SCGF) [27, 46]. Current ab initio many-body approaches have become possible to accurately describe more than one hundred fully interacting nucleons in a controlled way [7, 47].

The traditional spherical symmetry-conserving single-reference scheme of IMSRG is applicable only to closed-shell nuclei. To calculate open-shell nuclei, symmetry-breaking schemes have been developed, which include single- and multi-reference approaches [48–52]. To capture the strong collective correlations, Yuan et al. developed an ab initio deformed single-reference IMSRG approach for open-shell nuclei in the m-scheme Hartree–Fock (HF) basis, referred to as D-IMSRG [53]. Using the m-scheme, a single HF reference state can be constructed for any even–even nuclei. The deformed reference state efficiently includes the important configurations of the deformed nucleus and captures more correlations through symmetry restoration, which would be many-particle-many-hole excitations in the spherical scheme. The calculations under the axially deformed HF basis break the SU(2) rotational symmetry associated with angular momentum conservation. The broken rotation symmetry can be restored by angular momentum projection.

Next-generation rare isotope beam (RIB) facilities have the ability to produce most of the rare isotopes located at the edge of the nuclear landscape, thereby shedding light on the origin of elements, the fundamental problems of nuclear structure, and nuclear forces. However, providing theoretical descriptions of proton- or neutron-rich nuclei in these regions is challenging due to the complexity of theoretical methods and computational demands. As nuclei approach the dripline, the effects of single-particle long-distance asymptotic behavior and coupling to the continuum become crucial for understanding the open quantum systems [54]. The complex-energy Berggren basis provides an efficient framework to treat bound, resonant, and scattering continuum states on an equal footing [55, 56]. To include the coupling to the continuum, Hu et al. developed a Gamow IMSRG (G-IMSRG) [57] in the complex-energy Berggren basis. The advanced G-IMSRG is capable of describing the resonance and non-resonant continuum properties of weakly bound and unbound nuclei. The known heaviest Borromean halo ^{22}C is a challenging nucleus for many theoretical calculations [58–60]. The halo structure of ^{22}C can be clearly visualized by calculating the density distribution in which the continuum s channel plays a crucial role, and the low-lying resonant excited states in ^{22}C are predicted via the G-IMSRG [57].

Significant efforts have been made to develop theoretical frameworks in an alternative direction to provide a comprehensive description of dripline systems, which often exhibit exotic structures and decay modes. These approaches aim to unify the treatment of structure, decay, and reactions within a single framework. Although a fully comprehensive and microscopic model achieving this goal does not yet exist, substantial advances have been made over the past few decades [61–63]. Notably, in [64, 65], a method was demonstrated for integrating structural and reaction aspects starting from an ab initio framework. I. In this framework, each component of the three-body system is calculated using the no-core shell model (NCSM) in Jacobi coordinates. The inter-cluster motion is described using the resonating group method (RGM), which has been widely applied in nuclear reactions. Recent developments have also incorporated continuum effects, exemplified by the Gamow shell model coupled channel (GSM-CC) [54, 66] and Gamow coupled-channel (GCC) method [67, 68]. The former focuses on configuration mixing with self-consistent continuum effects [54, 69], whereas the latter emphasizes the open quantum nature of few-body valence nucleons coupled to a deformed core [68, 70, 71]. This review primarily focuses on the recent advancements in the GCC method and its applications to exotic decays in the dripline region.

This review is organized as follows. The basic IMSRG approach and its extensions are expounded in Sects. 2.1–2.4. The theory of GCC method is formulated in Sect. 2.5. Section 3 describes the main results of the corresponding IMSRG and GCC computations of atomic nuclei. Finally, a summary is presented in Sect. 4.

2 Outline of developed methods

In this section, the basic formulae for the developed IMSRG and GCC approaches are presented. Section 2.1 is dedicated to the main ideas and previous developments of IMSRG itself. The symmetry-breaking *m*-scheme D-IMSRG is introduced in Sect. 2.2 for open-shell nuclei applications. Another approach to treat the open-shell nuclei while preserving the spherical symmetry is the VS-IMSRG, which combines the shell model and IMSRG, as presented in Sect. 2.3. The G-IMSRG with the Berggren basis for the description of weakly bound and unbound nuclei is formulated in Sect. 2.4. Finally, the reaction-related GCC method and its extensions to deformed systems and time-dependent approaches are briefly introduced in Sects. 2.5 and 2.6.

2.1 The in-medium similarity renormalization group

The SRG is to evolve the Hamiltonian $H(s)$ to be band-diagonal by using the continuous unitary transformation as [34, 35]

$$H(s) = U(s)HU^{\dagger}(s) \equiv H^{\mathrm{d}}(s) + H^{\mathrm{od}}(s) \rightarrow H^{\mathrm{d}}(\infty), \tag{1}$$

where s denotes the so-called flow parameter and $H^{\mathrm{d}}(s)$ and $H^{\mathrm{od}}(s)$ are appropriately defined as the "diagonal" and "off-diagonal" parts of the Hamiltonian, respectively. Although the evolution should continue up to $s \rightarrow \infty$, a finite number of evolution steps is usually sufficient to make $H(s)$ approach the band-diagonal form of $H^{\mathrm{d}}(\infty)$.

Equation (1) expresses a general ideal. In practice, taking the derivative of Eq. (1), a flow equation is defined to evolve the Hamiltonian $H(0)$,

$$\frac{\mathrm{d}}{\mathrm{d}s}H(s) = [\eta(s), H(s)], \tag{2}$$

where the anti-Hermitian generator $\eta(s)$ is related to the unitary transformation $U(s)$ by

$$\eta(s) = \frac{\mathrm{d}U(s)}{\mathrm{d}s}U^{\dagger}(s) = -\eta^{\dagger}(s). \tag{3}$$

A commonly used generator is defined as

$$\eta(s) = \left[H^{\mathrm{d}}(s), H(s)\right] = \left[H^{\mathrm{d}}(s), H^{\mathrm{od}}(s)\right], \tag{4}$$

which guarantees that the off-diagonal coupling of H^{od} is driven exponentially to zero with increasing in the value of the flow parameter s [35]. In practice, the demand for strict diagonality is usually relaxed to band diagonality of the Hamiltonian matrix in a chosen basis, such as in relative momentum or harmonic oscillator (HO) spaces. In nuclear physics, the SRG is used to decouple the momentum or energy scales in free space to construct "soft" *NN* and 3*N* interactions, thereby rendering the nuclear Hamiltonian more suitable for ab initio many-body calculations [31, 33, 72–74].

The SRG is used to soften the nuclear force which has a hard core in free space. This renormalization can significantly accelerate ab initio calculations of nuclei. Another development of the SRG theory is the in-medium SRG (IMSRG) [36–38] which evolves the many-body Hamiltonian to block diagonal form. The decoupling between the lowest-energy ground state and excited states of the Hamiltonian directly provides the energy of the ground state of the nucleus. A distinct advantage of IMSRG, compared to the SRG free-space evolution, is its ability to approximately evolve $3, \ldots, A$-body operators using only two-body machinery. This simplification is primarily achieved through the use of normal ordering with respect to a reference state $|\Phi\rangle$, usually the Hartree–Fock (HF) state.

The intrinsic Hamiltonian of A-body nuclear system is expressed as

$$H = \sum_{i=1}^{A}\left(1 - \frac{1}{A}\right)\frac{\boldsymbol{p}_i^2}{2m} + \sum_{i<j}^{A}\left(v_{ij}^{NN} - \frac{\boldsymbol{p}_i \cdot \boldsymbol{p}_j}{mA}\right) + \sum_{i<j<k}^{A} v_{ijk}^{3N}, \tag{5}$$

where $\boldsymbol{p}_i$ is the nucleon momentum in laboratory coordinates and m is the nucleon mass, with v^{NN} and v^{3N} denoting the *NN* and 3*N* interactions, respectively. In order to generate the reference state in the IMSRG calculation, the HF equation for the intrinsic Hamiltonian Eq. (5) is first solved. The Wick's theorem is applied to normal order all operators starting from a general second-quantized Hamiltonian with two- and three-body interactions, with respect to the HF ground state.

$$\begin{aligned} H = & E_0 + \sum_{ij} f_{ij} : a_i^{\dagger} a_j : + \frac{1}{2!^2}\sum_{ijkl}\Gamma_{ijkl} : a_i^{\dagger} a_j^{\dagger} a_l a_k : \\ & + \frac{1}{3!^2}\sum_{ijklmn} W_{ijklmn} : a_i^{\dagger} a_j^{\dagger} a_k^{\dagger} a_n a_m a_l :, \end{aligned} \tag{6}$$

where E_0, f, Γ, and W correspond to the normal-ordered zero-, one-, two-, and three-body terms, respectively, given by

$$E_0 = \sum_i T_{ii} n_i + \frac{1}{2} \sum_{ij} (T_{ijij} + v^{NN}_{ijij}) n_i n_j + \frac{1}{6} \sum_{ijk} v^{3N}_{ijkijk} n_i n_j n_k, \quad (7)$$

$$f_{ij} = T_{ij} + \sum_k (T_{ikjk} + v^{NN}_{ikjk}) n_k + \frac{1}{2} \sum_{kl} v^{3N}_{ikljkl} n_k n_l, \quad (8)$$

$$\Gamma_{ijkl} = T_{ijkl} + v^{NN}_{ijkl} + \frac{1}{4} \sum_m v^{3N}_{ijmklm} n_m, \quad (9)$$

$$W_{ijklmn} = v^{3N}_{ijklmn}, \quad (10)$$

where $n_i = \theta(\varepsilon_{\mathrm{F}} - \varepsilon_i)$ represents the occupation numbers in the reference state $|\Phi\rangle$, with ε_{F} denoting the Fermi energy of the reference state and T representing the kinetic part of the Hamiltonian. From Eqs. (7)–(10), it is evident that all the zero-, one- and two-body parts of the Hamiltonian contain the in-medium effects from the free-space $3N$ interactions.

The exact treatment of the 3NF is computationally expensive. Therefore, the residual 3NF is usually neglected, which provides a reasonably good approximation in nuclear structure calculations. The omission of the residual normal-ordered three-body component of the Hamiltonian has been shown to result in only 1–2% discrepancy in ground-state and excited-states energies for light and medium-mass nuclei [16, 75]. The approximation of normal-ordered two-body (NO2B) for the Hamiltonian has been proved to be useful and beneficial in practical calculations, offering an efficient method to include 3NF effects in nuclear many-body calculations, thereby avoiding the computational burden of directly dealing with three-body operators.

Similar to the evolution of the Hamiltonian, the operators of other observables can also be evolved using the flow equation

$$\frac{\mathrm{d}}{\mathrm{d}s} O(s) = [\eta(s), O(s)]. \quad (11)$$

The Magnus expansion was usually used in matrix differential equations [76] and was applied to reformulate the IMSRG [77] for more efficient calculations. In the Magnus approach, the IMSRG transformation can be written as an exponential expression [76],

$$U(s) \equiv e^{\Omega(s)}. \quad (12)$$

The Magnus evolution operator $\Omega(s)$ works for both the Hamiltonian and other observable operators, which allows the derivation of the flow equation for the anti-Hermitian Magnus operator $\Omega(s)$,

$$\frac{\mathrm{d}\Omega}{\mathrm{d}s} = \sum_{k=0}^{\infty} \frac{B_k}{k!} \mathrm{ad}^k_{\Omega}(\eta), \quad (13)$$

where B_k denote the Bernoulli numbers and

$$\mathrm{ad}^0_{\Omega}(\eta) = \eta \quad (14)$$

$$\mathrm{ad}^k_{\Omega}(\eta) = \left[\Omega, \mathrm{ad}^{k-1}_{\Omega}(\eta)\right]. \quad (15)$$

In practical calculations, η and Ω are truncated along with their commutators at the two-body level, called the Magnus(2) approximation. The series of nested commutators generated by ad^k_{Ω} are recursively evaluated until a satisfactory convergence of the right-hand side of Eq. (13) is reached [77]. At each integration step, $U(s)$ is used to construct the Hamiltonian $H(s)$ via the Baker–Campbell–Hausdorff (BCH) formula

$$H(s) \equiv e^{\Omega}(s) H(0) e^{-\Omega}(s) = \sum_{k=0}^{\infty} \frac{1}{k!} \mathrm{ad}^k_{\Omega(s)}(H(0)). \quad (16)$$

The Magnus formulation offers a significant advantage, as it enables the evaluation of arbitrary observables by utilizing the final Magnus operator $\Omega(\infty)$,

$$O(\infty) \equiv e^{\Omega(\infty)} O(0) e^{-\Omega(\infty)}. \quad (17)$$

The computational effort for solving the IMSRG(2) flow equations is primarily dictated by the two-body flow equation, which exhibits polynomial complexity of $\mathcal{O}(N^6)$ based on the single-particle size N.

2.2 The deformed IMSRG

The use of deformations as degrees of freedom in nuclear many-body problems can make the calculations more efficient [78, 79]. The standard IMSRG conserves spherical symmetry with a single reference, which works for closed-shell nuclei. To calculate open-shell nuclei, symmetry-breaking schemes have been developed, including both single- and multi-reference approaches. The single-reference Hartree–Fock–Bogoliubov (HFB) IMSRG, which selects a single HFB state as the reference state, has been proposed [48]. The HFB quasiparticle state breaks the particle number conservation, necessitating that particle number projection be performed. To choose a reference state closer to the true solution, the multi-reference IMSRG with particle-number-projected spherical HFB [49, 50] has been suggested. Calculations based on the Bogoliubov quasiparticle states significantly complicate the formalism and increase computational costs. Using the m scheme, a single HF reference state can be constructed for any even–even nuclei, with the particle number conserved but rotational symmetry broken. This deformed reference state may better reflect the intrinsic structure of a deformed nucleus and capture more correlations through symmetry restoration, which would otherwise be many-particle-many-hole excitations in the spherical scheme. The expected symmetry preconsiderations, e.g., as in the symmetry-adapted approach [80, 81], provide an efficient way to capture the expected features of nuclear states of interest while simultaneously reducing the computational cost.

As indicated in Sect. 2.1, the standard IMSRG is limited to extracting the ground-state energy of a closed-shell nucleus. An extension of the IMSRG to the deformed scheme would be useful for the description of open-shell nuclei. Therefore, we developed the D-IMSRG method [53] within the deformed HF basis, i.e., the m-scheme HF basis. First, the axially deformed HF equation of the even–even nucleus is solved within the spherical HO basis. Under the j-scheme, the initial Hamiltonian is typically expressed in the spherical HO basis. Using the Wigner–Eckart theorem, the matrix elements of operators, including the Hamiltonian in the j-scheme, can be converted to the matrix elements in the m-scheme,

$$\left\langle \alpha' j' m' \middle| O_{kq} \middle| \alpha j m \right\rangle = \left\langle jmkq \mid j'm' \right\rangle \times \frac{1}{\sqrt{2j'+1}} \left\langle \alpha' j' \middle\| O_k \middle\| \alpha j \right\rangle, \tag{18}$$

where $|\alpha jm\rangle$ are quantum states with good angular momentum j and projection m. The quantity α contains all other quantum numbers needed to completely specify the quantum state. O_{kq} is a spherical tensor of rank k; $\langle jmkq \mid j'm'\rangle$ is the Clebsch–Gordan coefficient; and $\left\langle \alpha' j' \middle\| O_k \middle\| \alpha j \right\rangle$ denotes the reduced matrix elements. The one-, two-, and three-body matrix elements can thus be converted from j-scheme to m-scheme through Eq. (18). The m-scheme HF single-particle levels obtained are twofold degenerate with respect to the angular momentum projection quantum number m of the orbital (i.e., the energies are the same with respect to $\pm m$). Filling the deformed HF single-particle levels up to the Fermi surfaces of neutrons and protons in $\pm m$ pairing from low to high $|m|$, keeps the axial, parity, and time-reversal symmetries of the even–even ground state, thereby creating an oblate or prolate deformed HF reference state [82]. Subsequently, the intrinsic A-body Hamiltonian in Eq. (5) is normal ordered with respect to the deformed A-dependent reference state $|\Phi\rangle$ (i.e., the m-scheme HF ground state of the target nucleus). The off-diagonal parts of the Hamiltonian are consistent with the standard IMSRG, and the flow equations are evolved using the Magnus expansion Eqs. (16)–(17).

Subsequently, the ground-state energy and other observables can be calculated using the D-IMSRG ground-state wave function $|\Psi\rangle = e^{-\Omega}|\Phi\rangle$ (here $|\Phi\rangle$ is the deformed HF reference state of the nucleus) expressed as

$$E = \langle\Psi|H|\Psi\rangle = \langle\Phi|e^{\Omega}He^{-\Omega}|\Phi\rangle = \langle\Phi|\tilde{H}|\Phi\rangle, \tag{19}$$

$$O = \langle\Psi|O|\Psi\rangle = \langle\Phi|e^{\Omega}Oe^{-\Omega}|\Phi\rangle = \langle\Phi|\tilde{O}|\Phi\rangle. \tag{20}$$

In the D-IMSRG, the reference state is just the ground state of the deformed even–even nucleus. However, performing exact symmetry restoration of the D-IMSRG wave function is mathematically cumbersome and computationally expensive due to the exponential increase of configurations in projecting the wave function $|\Psi\rangle = e^{-\Omega}|\Phi\rangle$.

Therefore, an HF projection correction is introduced as a first approximation, to account for the angular momentum projection effect. The projection correction to the ground-state energy is estimated by

$$\Delta E_{\mathrm{proj}} = \frac{\langle\Phi|HP|\Phi\rangle}{\langle\Phi|P|\Phi\rangle} - \frac{\langle\Phi|H|\Phi\rangle}{\langle\Phi|\Phi\rangle}, \tag{21}$$

where $P^J_{MM'} = \frac{2J+1}{8\pi^2}\int \mathrm{d}\omega D^{J*}_{MM'}(\omega)R(\omega)$ is the angular momentum projection operator. This provides a D-IMSRG ground-state energy given by $E + \Delta E_{\mathrm{proj}}$ with the projection correction estimated by the HF wave function (here E is obtained by Eq. (19), that is, the ground-state energy without the projection).

A deformed coupled-cluster calculation has estimated that the angular-momentum projection of the HF state reduced the HF energy by approximately 3–5 MeV in the *sd* shell [82], corresponding to the static correlation, which is not size extensive. Since modern ab initio calculations already include some of the correlations associated with the projection, the energy correction obtained by projecting the ab initio wave function would be slightly smaller than the HF projection correction [82, 83].

In the spherical j-scheme, single-particle levels within the same j shell are degenerate. However, this degeneracy is broken with the onset of deformation although a twofold degeneracy with respect to $\pm m$ persists in axially symmetric shapes, significantly increasing the model-space dimension. The dimension of D-IMSRG calculation depends on the nucleon number A and basis-space size N_{shell} (the number of spherical HO major shells considered in solving the deformed HF). For ^{40}Mg, the number of D-IMSRG Hamiltonian matrix elements already exceeds 10^9 at $N_{\mathrm{shell}} = 10$. Nonetheless, such a large model space may still not be sufficient to make the calculation converged. To estimate the converged ground-state energy, a simple exponential fitting method was applied with respect to N_{shell} to extrapolate the D-IMSRG result to an infinite basis space, similar to the ones used in NCSM [16, 84–87] and multi-reference IMSRG [19] calculations,

$$E(N_{\mathrm{shell}}) = b_0 + b_1 \exp(-b_2 N_{\mathrm{shell}}), \tag{22}$$

where b_0, b_1, and b_2 are the fitting parameters. The value of $b_0 \equiv E(N_{\mathrm{shell}} \to \infty)$ provides the estimate for the fully converged energy.

2.3 The valence-space IMSRG

The spherical *j*-scheme IMSRG can only treat closed-shell nuclei. The *m*-scheme D-IMSRG was designed to calculate open-shell nuclei. Unfortunately, the D-IMSRG does not conserve the angular momentum, and the exact angular-momentum projection D-IMSRG has not been available.

The nuclear shell model (SM) has served as one of the most powerful theoretical and computational tools for nuclear structure calculations [38, 88–91]. In the SM, valence nucleons move in the mean field generated by the inert core and interact via residual effective interactions. While the SM has been used predominantly in a phenomenological context [91, 92], there have been efforts dating back to decades ago to derive shell-model parameters based on a realistic interaction between nucleons [93, 94], the ab initio effective shell-model interactions. For open-shell systems, in addition to solving the full A-body problem, such as the D-IMSRG mentioned in Sect. 2.2, it is beneficial to follow the shell-model paradigm to construct and diagonalize the effective Hamiltonian in which the active degrees of freedom are A_v valence nucleons confined to a few orbitals near the Fermi level. As for the IMSRG, a valence-space effective interaction can be derived using the spherical symmetry-conserving single-reference IMSRG at a shell closure to perform ab initio shell-model calculations for open-shell nuclei. This method, which combines the IMSRG and SM, is referred to as the VS-IMSRG [39].

The utility of the IMSRG lies in its flexibility to customize the definition of H^{od} to address specific problems. For the ground state of closed-shell nuclei, all terms that couple the reference state $|\Phi\rangle$ to the rest of the Hilbert space can be eliminated, as in the standard IMSRG. For open-shell nuclei, $|\Phi_v\rangle$ is decoupled from states containing non-valence states. This can be achieved by defining the H^{od} using the following matrix elements,

$$H^{\mathrm{od}} = \left\{ f_{ph}, f_{pp'}, f_{hh'}, \Gamma_{pp'hh'}, \Gamma_{pp'vh}, \Gamma_{pqvv'} \right\} + \text{H.c.}, \tag{23}$$

where $p = v, q$. These off-diagonal parts of the generators evolve the Hamiltonian to diagonal H^{d} form, where states outside the valence space are decoupled using the flow equation, as illustrated in Fig. 1, non-perturbatively satisfying the decoupling equation:

$$PH^{\mathrm{d}}(\infty)Q = QH^{\mathrm{d}}(\infty)P = 0, \tag{24}$$

with $P = \sum_v |\Phi_v\rangle\langle\Phi_v|$ and $Q = 1 - P$. After the evolution is complete, the effective shell-model Hamiltonian is obtained. The last step is to use the SM code, such as KSHELL [95], to diagonalize the effective Hamiltonian and express it as a reduced eigenvalue problem in the valence-particle space.

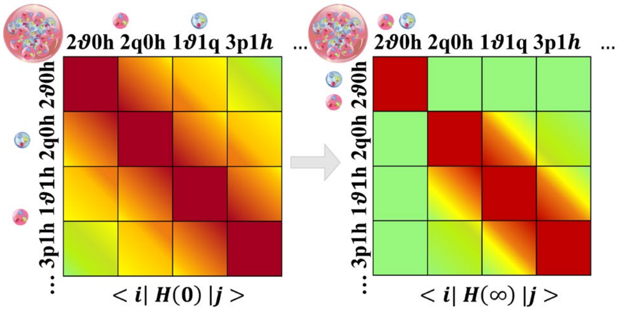

Fig. 1 (Color online) Schematic illustration of the VS-IMSRG decoupling from the initial Hamiltonian $H(0)$ to obtain the final Hamiltonian $H(\infty)$ for the two valence nucleons

The current VS-IMSRG is at two-body approximation without explicitly considering 3NF or three-body correlations. To reduce the residual 3NF effect, a fractional filling of open-shell orbitals in an open-shell nucleus, named ensemble normal ordering (ENO), has been suggested [40]. Using the ENO approximation of the VS-IMSRG, nucleus-dependent valence-space effective Hamiltonian and effective operators of other observables can be obtained.

2.4 The Gamow IMSRG with coupling to continuum

Weakly bound and unbound nuclei belong to the category of open quantum systems, where coupling to the particle continuum profoundly affects the system behavior [96, 97]. Many novel phenomena, including halos [98, 99], genuine intrinsic resonances [100, 101], and new collective modes [102–104], have been observed or predicted in exotic nuclei. However, the majority of IMSRG calculations are performed within the HO or real-energy HF basis. Here the real-energy HF means that the HF approach is performed under the HO basis, which is bound and localized and hence isolated from the environment of unbound scattering states because of the Gaussian falloff of the HO functions. Similarly, the real-energy HF basis cannot include the continuum effect in IMSRG calculations.

The complex-energy Berggren basis offers an elegant framework for treating bound, resonant, and scattering continuum states on an equal footing [55, 56]. This basis is a generalization of the standard completeness relation from the real-energy axis to the complex-energy plane. Completeness encompasses a finite set of bound and resonance states together with a complex-energy scattering continuum:

$$\sum_n u_n(E_n,r)u_n(E_n,r') + \int_L \mathrm{d}E\, u(E,r)u(E,r') = \delta(r-r'), \tag{25}$$

where

$$u_n(E_n,r) \sim O_l(k_n r) \sim \mathrm{e}^{\mathrm{i}k_n r}. \tag{26}$$

Here, $k_n = \mathrm{i}\kappa_n(\kappa_n > 0)$ for bound states and $k_n = \gamma_n - \mathrm{i}\kappa_n(\kappa_n, \gamma_n > 0)$ for decaying resonances located in the fourth quadrant of the complex-momentum (complex-k) plane.

In practical applications, it is more convenient to express Eq. (25) in momentum space,

$$\sum_{n\in(b,d)} |u_n\rangle\langle u_n| + \int_{L^+} |u(k)\rangle\langle u(k)|\mathrm{d}k = 1. \tag{27}$$

As depicted in Fig. 2, bound and resonant states appear as poles of the scattering matrix within the complex-k plane, and the scattering continuum is represented by the blue contour. Within the Berggren basis, the GSM [23, 100, 101, 105–115] and complex coupled cluster [18, 116] methods have been well developed and widely applied to the calculations of weakly bound and unbound nuclei.

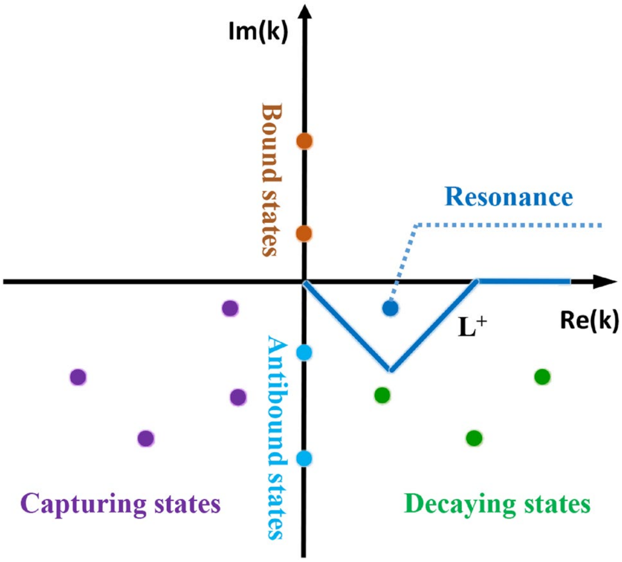

Fig. 2 (Color online) Location of one-body states in the complex-k plane. The Berggren completeness relation in Eq. (25) involves the bound states (brown-filled circles) lying on the imaginary k-axis, scattering states lying on the contour (solid blue line), and decaying resonant states (blue-filled circles) in the fourth quarter of the complex-k plane lying between the real axis and scattering contour. The capturing states (purple-filled circles) and antibound states (cyan-filled circles) are not included in the present completeness relation

For calculations within the Gamow–Berggren framework, selecting an appropriate one-body potential is essential for generating resonance and the continuum Berggren basis, frequently using the phenomenological Woods–Saxon potential [100, 101, 105, 111, 117]. In our approach, we used the Gamow Hartree–Fock (GHF) method with chiral potentials to produce an ab initio Berggren single-particle basis, which is convenient for computing the Berggren basis using an analytical continuation of Schrödinger's equation in complex-k space. The complex-k single-particle GHF equation is formulated as follows:

$$\frac{\hbar^2 k^2}{2\mu}\psi_i(k) + \int_{L^+} \mathrm{d}k' k'^2 U(ljk'k)\psi_i(k') = e_i\psi_i(k), \tag{28}$$

where $\mu = m/\left(1 - \frac{1}{A}\right)$, and $k(k')$ is defined on the scattering contour. $U(ljk'k)$ is the GHF single-particle potential,

$$U(ljk'k) = \langle k|U|k'\rangle = \sum_{\alpha\beta}\langle k'|\alpha\rangle\langle\alpha|U|\beta\rangle\langle\beta|k\rangle, \tag{29}$$

where l, j are the orbital and total angular momenta of a single-particle orbital, respectively. Greek letters denote HO states, indicating that $\langle\beta|k\rangle$ is the HO basis wave functions $|\beta\rangle$ expressed in the complex-k plane

$$\langle\beta|k\rangle = (-i)^{2n+l} e^{-l/2b^2k^2}(bk)^l \times \sqrt{\frac{2n!b^3}{\Gamma(n+l+3/2)}} L_n^{l+1/2}(b^2k^2). \tag{30}$$

Here $L_n^{l+1/2}$ denotes the generalized Laguerre polynomial; $b = \sqrt{\hbar/m\omega}$; and ω is the frequency of the oscillator basis. Since $L_n^{l+1/2}$ is analytic, it can be extended to the complex momentum space, expressing its real part as

$$\mathrm{Re}\left[L_n(x+iy)\right] = \sum_{j=0}^{\left\lfloor \frac{n}{2} \right\rfloor} \frac{(-1)^j y^{2j}}{(2j)!} L_{n-2}^{2j}(x), \tag{31}$$

and its imaginary part as

$$\mathrm{Im}\left[L_n(x+iy)\right] = \sum_{j=0}^{\left\lfloor \frac{n-1}{2} \right\rfloor} \frac{(-1)^{j-1} y^{2j+1}}{(2j+1)!} L_{n-2j-1}^{2j+1}(x), \tag{32}$$

where x and y represent the real and imaginary parts of b^2k^2, respectively; $\langle\alpha|U|\beta\rangle$ is the HF single-particle potential which can be obtained by solving the real-energy HF equation in the HO basis

$$\langle\alpha|U|\beta\rangle = \sum_{i=1}^{A}\sum_{\gamma\delta}\left\langle\alpha\gamma\middle|v^{NN}\middle|\beta\delta\right\rangle D^{*}_{\gamma i}D_{\delta i} + \frac{1}{2}\sum_{i,j=1}^{A}\sum_{\gamma\delta\epsilon\zeta}\left\langle\alpha\gamma\epsilon\middle|v^{3N}\middle|\beta\delta\zeta\right\rangle D^{*}_{\gamma i}D_{\delta i}D^{*}_{\epsilon j}D_{\zeta j}, \tag{33}$$

where D is the coefficient of the HF single-particle state. In numerical calculations, the GHF equation is solved using the Gauss-Legendre quadrature scheme [107, 112, 118] with discrete points on the contour L^{+},

$$\frac{\hbar^2 k_\alpha^2}{2\mu}\psi_i(k_\alpha) + \sum_\beta \omega_\beta k_\beta^2 \langle k_\alpha|U|k_\beta\rangle \psi_i(k_\beta) = e_i\psi_i(k_\alpha). \tag{34}$$

Here k_α (k_β) are the discrete momentum points, and ω_α (ω_β) are the corresponding Gauss-Legendre quadrature weights. We define

$$\psi_i'(k_\alpha) = \psi_i(k_\alpha)k_\alpha\sqrt{\omega_\alpha}. \tag{35}$$

Then, Eq. (34) can be written as

$$\sum_\beta h_{\alpha\beta}\psi_i'(k_\beta) = e_i\psi_i'(k_\alpha), \tag{36}$$

with

$$h_{\alpha\beta} = \frac{\hbar^2}{2\mu}k_\alpha^2\delta_{\alpha\beta} + \sqrt{\omega_\alpha\omega_\beta}\langle k_\alpha|U|k_\beta\rangle. \tag{37}$$

The bound, resonant, and continuum GHF basis can be obtained by diagonalizing the complex-energy in Eq. (36).

Within the GHF basis, the G-IMSRG calculations can be conducted. Notably, the Hamiltonian in real-energy space is Hermitian, $H = H^\dagger$. Therefore, in practice, the similarity transformation $U(s)$ is a unitary transformation, satisfying $U(s)U^\dagger(s) = U(s)U^{-1}(s) = 1$, and $\eta(s) = \frac{\mathrm{d}U(s)}{\mathrm{d}s}U^\dagger(s) = -\eta^\dagger(s)$ is the anti-Hermitian generator. However, in the G-IMSRG framework, the Hamiltonian is complex symmetric, $H = H^{\mathrm{T}}$ (here T indicates the transpose). Therefore, employing a continuous orthogonal transformation, $U(s)U^{\mathrm{T}}(s) = U(s)U^{-1}(s) = 1$, and the Hamiltonian $H(s)$ can be transformed into a band or block diagonal form,

$$H(s) = U(s)H(0)U^{\mathrm{T}}(s). \tag{38}$$

Correspondingly, the generator $\eta(s)$ becomes

$$\eta(s) = \frac{\mathrm{d}U(s)}{\mathrm{d}s}U^{\mathrm{T}}(s) = -\eta^{\mathrm{T}}(s). \tag{39}$$

The G-IMSRG method can directly compute the ground state of a closed-shell nucleus by decoupling the Hamiltonian from the excitations above the closed-shell Fermi surface. To handle open-shell nuclei or excited states, we employed G-IMSRG using the equation-of-motion (EOM) approach [119]. This approach offers a useful alternative to the shell model strategy for calculating excited states, especially when extended valence spaces lead to prohibitively large shell-model basis dimensions. Within the EOM framework, the Schrödinger equation is rewritten using ladder operators, which create excited eigenstates from the exact ground state,

$$H|\Psi_n\rangle = E_n|\Psi\rangle \quad \longrightarrow \quad HX_n^\dagger|\Psi_0\rangle = E_nX_n^\dagger|\Psi_0\rangle, \tag{40}$$

where $X_n^\dagger$ is given by the dyadic product $|\Psi_n\rangle\langle\Psi_0|$. Further rewriting Eq. (40) as EOM

$$[H, X_n^\dagger]|\Psi_0\rangle = (E_n - E_0)X_n^\dagger|\Psi_0\rangle \equiv \omega_n X_n^\dagger|\Psi_0\rangle. \tag{41}$$

The amplitudes of $X_n^\dagger$ are determined by solving a generalized eigenvalue problem [120].

Coupling EOM methods with G-IMSRG is natural, as the reference state $|\Phi_0\rangle$ corresponds to the ground state of $\bar{H} \equiv U(\infty)HU^{\mathrm{T}}(\infty)$. Multiplying Eq. (41) by $U(\infty)$ and recalling that

$$U(\infty)|\Psi_0\rangle = |\Phi_0\rangle, \tag{42}$$

we obtain the similarity transformed EOM

$$[\bar{H}, \bar{X}_n^\dagger]|\Phi_0\rangle = \omega_n\bar{X}_n^\dagger|\Phi_0\rangle, \tag{43}$$

where $\bar{X}_n^\dagger \equiv U(\infty)X_n^\dagger U^{\mathrm{T}}(\infty)$. The solutions $\bar{X}_n^\dagger$ can then be used to obtain the eigenstates of the unevolved Hamiltonian via

$$|\Psi_n\rangle = U^T(\infty)\bar{X}_n^\dagger|\Phi_0\rangle. \tag{44}$$

Currently, in our applications, we include up to $2p2h$ excitations in the ladder operator [120]

$$\bar{X}_n^\dagger = \sum_{ph}\bar{X}_{ph}^{(n)}\left\{a_p^\dagger a_h\right\} + \frac{1}{4}\sum_{pp'hh'}\bar{X}_{pp'hh'}^{(n)}\left\{a_p^\dagger a_{p'}^\dagger a_{h'}a_h\right\}. \tag{45}$$

In principle, the EOM ladder operator can include any excitation rank up to $ApAh$, which would constitute an exact diagonalization of $\bar{H}$ and can be computationally expensive. In practical applications, the EOM-G-IMSRG method is commonly employed in an approximative systematically improbable form, referred to as EOM-G-IMSRG(m, n), where m and n denote the truncation level in EOM and G-IMSRG, respectively. The calculations in the present work were performed using the EOM-G-IMSRG(2,2) approximation.

2.5 The Gamow coupled-channel method

To provide a thorough description of open quantum systems, the GCC method [67, 68, 70] has been advanced as an alternative approach, focusing on the few-body decay processes influenced by continuum and structural factors [121, 122]. The methodology involves constructing a robust three-body framework, utilizing the Berggren basis [55]. As elucidated in Sect. 2.4, the Berggren basis is specifically designed to incorporate continuum effects, thereby facilitating the analysis of weakly bound and unbound nuclear systems.

2.5.1 Spherical system with an inert core

In the context of the three-body GCC model, the nucleus comprises a core and two valence nucleons or clusters. The GCC Hamiltonian is formulated as follows:

$$H = \sum_{i=1}^{3} \frac{\hat{\vec{p}}_i^{\,2}}{2m_i} + \sum_{i>j=1}^{3} V_{ij}(\vec{r}_{ij}) - \hat{T}_{\text{c.m.}}, \tag{46}$$

where V_{ij} denotes the interaction between clusters i and j, and $\hat{T}_{\text{c.m.}}$ represents the kinetic energy of the center-of-mass. Each i-th cluster ($i = c, n_1, n_2$) is characterized by its position vector $\vec{r}_i$ and linear momentum $\vec{k}_i$. To accurately describe three-body asymptotics and eliminate the spurious center-of-mass motion, it is advantageous to utilize the relative (Jacobi) coordinates:

$$\begin{aligned} \vec{x} &= \sqrt{\mu_x}(\vec{r}_{i_1} - \vec{r}_{i_2}), \\ \vec{y} &= \sqrt{\mu_y}\left(\frac{A_{i_1}\vec{r}_{i_1} + A_{i_2}\vec{r}_{i_2}}{A_{i_1} + A_{i_2}} - \vec{r}_{i_3}\right), \end{aligned} \tag{47}$$

where $i_1 = n_1, i_2 = n_2$ and $i_3 = c$ for T-coordinates, whereas $i_1 = n_2, i_2 = c$ and $i_3 = n_1$ for Y-coordinates, as depicted in Fig. 3. Here, A_i represents the mass number of the i-th cluster; $\mu_x = \frac{Ai_1A_{i_2}}{A_{i_1}+A_{i_2}}$ and $\mu_y = \frac{(A_{i_1}+A_{i_2})A_{i_3}}{A_{i_1}+A_{i_2}+A_{i_3}}$ are the reduced masses associated with $\vec{x}$ and $\vec{y}$, respectively. For analytical convenience, the hyperradius $\rho = \sqrt{x^2 + y^2}$, which remains invariant across different Jacobi coordinate transformations, is introduced.

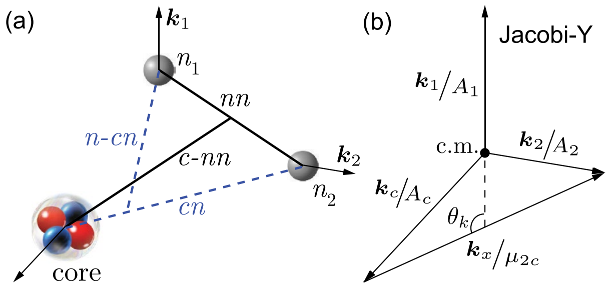

Fig. 3 (Color online) Illustration of the coordinate and momentum configurations in a core + nucleon + nucleon system: **a** Jacobi T (solid lines) and Y (dashed lines) coordinates, where the former is used to describe the interactions between the nucleons (n_1 and n_2) and the latter for interactions involving the core (c). **b** Corresponding momentum scheme within the c.m. frame. Here, A denotes the mass number; μ_{ij} represents the reduced mass between clusters i and j; and k_1, k_2, and k_c indicate the momenta of nucleons n_1, n_2, and core c, respectively. The figure is taken from [70]

Experimental measurements in the momentum space necessitate the definition of relative momenta as follows:

$$\begin{aligned} \vec{k}_x &= \mu_x\left(\frac{\vec{k}_{i_1}}{A_{i_1}} - \frac{\vec{k}_{i_2}}{A_{i_2}}\right), \\ \vec{k}_y &= \mu_y\left(\frac{\vec{k}_{i_1} + \vec{k}_{i_2}}{A_{i_1} + A_{i_2}} - \frac{\vec{k}_{i_3}}{A_{i_3}}\right). \end{aligned} \tag{48}$$

In the absence of c.m. motion, it is evident that $\sum_i \vec{k}_i = 0$, and notably, $\vec{k}_y$ is oriented in the opposite direction to $\vec{k}_{i_3}$. The angles θ_k and θ'_k represent the opening angles of the vectors $(\vec{k}_x, \vec{k}_y)$ in T- and Y-Jacobi coordinates, respectively (refer to Fig. 3). For example, in the scenario of two-nucleon decay, the kinetic energy associated with the relative motion of the emitted nucleons is expressed as $E_{\text{pp/nn}} = \frac{\hbar^2 k_x^2}{2\mu_x}$, with $E_{\text{core-p/n}}$ pertaining to the kinetic energy of the core-nucleon pair. The distribution types T $(\theta_k, E_{\text{pp/nn}})$ and Y $(\theta'_k, E_{\text{core-p/n}})$ elucidate the nucleon–nucleon correlations and provide insights into the structural dynamics of the progenitor nucleus. The total momentum k is defined as $\sqrt{\frac{k_x^2}{\mu_x} + \frac{k_y^2}{\mu_y}}$, which asymptotically approaches $\frac{\sqrt{2mQ_{2\text{p}/2\text{n}}}}{\hbar}$ as time progresses, where $Q_{2\text{p}/2\text{n}}$ is the two-nucleon decay energy derived from the binding energy difference between parent and daughter nuclei.

The presence of Pauli forbidden states in three-body models represents a challenge arising from the lack of antisymmetrization between core and valence particles. To address this issue, the orthogonal projection method [123–125], which entails the inclusion of a Pauli operator in the GCC Hamiltonian, was adopted and formulated as:

$$\hat{Q} = \Lambda \sum_{c} |\varphi^{j_c m_c}\rangle\langle\varphi^{j_c m_c}|, \tag{49}$$

where Λ is a large constant, and $|\varphi^{j_c m_c}\rangle$ represents a two-body state comprising forbidden single-particle (s.p.) states of core nucleons. By setting Λ to high values, Pauli forbidden states are elevated to higher energies, which effectively suppresses their influence within the physical spectrum of the system.

This standard projection technique [67] may introduce minor numerical errors in the asymptotic region because of coordinate transformations. The supersymmetric transformation method [125–127] offers an alternative solution for the exclusion of Pauli-forbidden states. This method employs an auxiliary repulsive "Pauli core" within the original core-proton interaction, thereby effectively eliminating the influence of Pauli-forbidden states from the system.

The total wave function is expressed using hyperspherical harmonics as:

$$\Psi^{JM\pi}(\rho,\Omega_5)=\rho^{-5/2}\sum_{\gamma K}\psi^{J\pi}_{\gamma K}(\rho)\mathcal{Y}^{JM}_{\gamma K}(\Omega_5), \tag{50}$$

where K denotes the hyperspherical quantum number. The set $\gamma=\{s_1,s_2,s_3,S_{12},S,\ell_x,\ell_y,L\}$ encapsulates the quantum numbers other than K. Here, s represents spin and ℓ denotes orbital angular momentum. The function $\psi^{J\pi}_{\gamma K}(\rho)$ specifies the hyperradial wave function, and $\mathcal{Y}^{JM}_{\gamma K}(\Omega_5)$ represents the corresponding hyperspherical harmonic [125].

The resulting Schrödinger equation for the hyperradial wave functions can be written as a set of coupled-channel equations:

$$\begin{aligned}&\left[-\frac{\hbar^2}{2m}\left(\frac{\mathrm{d}^2}{\mathrm{d}\rho^2}-\frac{(K+3/2)(K+5/2)}{\rho^2}\right)-\tilde{E}\right]\psi^{J\pi}_{\gamma K}(\rho)\\&\quad+\sum_{K'\gamma'}V^{J\pi}_{K'\gamma',K\gamma}(\rho)\psi^{J\pi}_{\gamma'K'}(\rho)\\&\quad+\sum_{K'\gamma'}\int_0^\infty W_{K'\gamma',K\gamma}(\rho,\rho')\psi^{L\pi}_{\gamma'K'}(\rho')\mathrm{d}\rho'=0,\end{aligned} \tag{51}$$

where

$$V^{L\pi}_{K'\gamma',K\gamma}(\rho)=\langle\mathcal{Y}^{JM}_{\gamma'K'}|\sum_{i>j=1}^{3}V_{ij}(\vec{r}_{ij})|\mathcal{Y}^{JM}_{\gamma K}\rangle \tag{52}$$

and

$$W_{K'\gamma',K\gamma}(\rho,\rho')=\langle\mathcal{Y}^{JM}_{\gamma'K'}|\hat{Q}|\mathcal{Y}^{JM}_{\gamma K}\rangle \tag{53}$$

is the non-local potential generated by the Pauli projection operator, as defined in Eq. 49.

To properly treat the positive-energy continuum space, the Berggren expansion technique is utilized for the hyperradial wave function:

$$\psi^{J\pi}_{\gamma K}(\rho)=\sum_{\mathrm{n}}C^{J\pi M}_{\gamma\mathrm{n}K}\mathcal{B}^{J\pi}_{\gamma\mathrm{n}}(\rho), \tag{54}$$

where $\mathcal{B}^{J\pi}_{\gamma\mathrm{n}}(\rho)$ denotes an s.p. state within the Berggren ensemble [55] (detailed in Sect. 2.4). To compute radial matrix elements using the Berggren basis, exterior complex scaling [128] is employed, whereby integrals are evaluated along a complex radial trajectory:

$$\begin{aligned}\langle\mathcal{B}_{\mathrm{n}}|V(\rho)|\mathcal{B}_{\mathrm{m}}\rangle&=\int_0^R\mathcal{B}_{\mathrm{n}}(\rho)V(\rho)\mathcal{B}_{\mathrm{m}}(\rho)\mathrm{d}\rho\\&\quad+\int_0^{+\infty}\mathcal{B}_{\mathrm{n}}(R+\rho e^{i\theta})V(R+\rho e^{i\theta})\mathcal{B}_{\mathrm{m}}(R+\rho e^{i\theta})\mathrm{d}\rho.\end{aligned} \tag{55}$$

For potentials that decay as $O(1/\rho^2)$ (such as the centrifugal potential) or more rapidly (such as the nuclear potential), R should be large enough to circumvent all singularities, with the scaling angle θ selected to ensure that the integrals converge (see [129] for further details). Since the Coulomb potential is not square-integrable, its matrix elements diverge when the complex momenta $k_n=k_m$. To address this, the "off-diagonal method" introduced in [130], where a slight offset $\pm\delta k$ is added to the linear momenta of the involved scattering wave-functions, was applied to facilitate the convergence of the resulting diagonal Coulomb matrix elements. The complex-momentum representation has also been adopted in other methods, e.g., in mean-field calculations [131, 132], to describe the continuum effect.

2.5.2 Deformed core

The fact that the open-shell nuclei are often accompanied by deformation, particularly around the dripline region, substantially changes the corresponding nuclear structure and affects the decay process. To this end, GCC method was extended to the deformed system by allowing the pair of nucleons to couple to the collective states of the core. Consequently, the wave function of the parent nucleus can be written as $\Psi^{J\pi}=\sum_{J_p\pi_p j_c\pi_c}\left[\Phi^{J_p\pi_p}\otimes\phi^{j_c\pi_c}\right]^{J\pi}$, where $\Phi^{J_p\pi_p}$ and $\phi^{j_c\pi_c}$ are the wave functions of the two valence protons and the core, respectively. Similar to the spherical case, the wave function $\Phi^{J_p\pi_p}$ for the valence nucleons is constructed in Jacobi coordinates using the hyperspherical harmonics $\mathcal{Y}^{J_pM}_{\gamma K}(\Omega)$ for the hyperangle part, and the hyperradial part $\psi_{\gamma K}(\rho)$ is expanded in the Berggren ensemble [67, 133].

In the deformed case, the core+p+p Hamiltonian of GCC is

$$H=\sum_{i=c,p_1,p_2}^{3}\frac{\hat{\vec{p}}_i^{\,2}}{2m_i}+\sum_{i>j=1}^{3}V_{ij}(\vec{r}_{ij})+\hat{H}_c-\hat{T}_{\mathrm{c.m.}}. \tag{56}$$

This definition is similar to Eq. 46, except that $\hat{H}_c$ is the core Hamiltonian represented by excitation energies of the core $E^{j_c\pi_c}$. For nuclei exhibiting small shape deformations, the vibrational coupling model is utilized, following the methodologies outlined in [134, 135]. Conversely, for large quadrupole deformations, rotational coupling is employed, consistent with the non-adiabatic approach to deform proton emitters as in [136, 137]. This approach allows for the differentiated treatment of nuclear dynamics depending on the extent of deformation, thereby enhancing the accuracy of theoretical predictions in nuclear structure analysis.

By employing hyperspherical harmonics and the Berggren basis, the Schrödinger equation can be formulated as a coupled-channel equation. This formulation incorporates couplings not only among the hyperspherical basis states but also among the collective states of the core. The resulting complex eigenvalues provide information about the resonance energies and decay widths. However, in the case of medium-mass nuclei, proton decay widths typically fall below the numerical precision of calculations. Nevertheless, decay widths can be estimated using the current expression presented in [138], as demonstrated in previous works [67, 139, 140]. According to R-matrix theory, if the contribution from the off-diagonal part of the Coulomb interaction in the asymptotic region is neglected, the hyperradial wave function of the resonance, $\psi_{\gamma K}(\rho)$, is proportional to the outgoing Coulomb function $H^{+}_{K+3/2}(\eta_{\gamma K}, k_p\rho)$ [141–143]. By assuming a small decay width and adopting the expression $\psi'/\psi = k_p H^{+'}/H^{+}$ [136, 137], the numerical derivative of the small-wave function in the asymptotic region that appears in the original current expression can be avoided, thereby significantly enhancing numerical precision [144].

2.6 Time-dependent approach

To tackle the decay process, a time-dependent formalism was developed, to allow precise, numerically stable, and transparent investigations of a broad range of phenomena, such as configuration evolution [145], decay rates [146], and fission [147]. For two-nucleon decay, the measured interparticle correlations can be interpreted by propagating the solutions over long times. Despite previous efforts in this direction [148–150], capturing the asymptotic correlation of emitted particles still requires a precise description of the resonance wave function at large distances. To this end, we utilized the complex-momentum state $\Psi_0^{J\pi}$ obtained using the GCC method. This state can be decomposed into real-momentum scattering states using the Fourier–Bessel series expansion in the real-energy Hilbert space [151]. The resulting wave packet is propagated by the time evolution operator through the Chebyshev expansion [152, 153]:

$$e^{-i\frac{\hat{H}}{\hbar}t} = \sum_{n=0}^{\infty}(-i)^n\left(2-\delta_{n0}\right)J_n(t)T_n(\hat{H}/\hbar), \tag{57}$$

where J_n are the Bessel functions of the first kind and T_n are the Chebyshev polynomials.

The time evolution was limited to the real momentum space, to restore the Hermitian property of the Hamiltonian matrix and ensure conservation of total density. Our implementation of the time-dependent approach is based on the integral equation, which allows maintaining high numerical precision by utilizing the Chebyshev expansion's good convergence rate [153, 154]. Furthermore, the evolving wave packet has an implicit cutoff at large distances, preventing the divergence of the Coulomb interaction in momentum space. In practice, we considered interactions within a sphere of radius of approximately 500 fm, and the wave function remained defined in momentum space beyond this cutoff, preventing unwanted reflections at the boundary.

3 The calculations and discussions

In this section, we primarily review the calculations by our developed D-IMSRG, G-IMSRG, and GCC. Section 3.1 presents the ground-state energies of ^{8,10}Be isotopes as benchmark, along with the ground-state energies and charge radii of even–even nuclei from light beryllium to medium-mass magnesium isotopes using D-IMSRG. In Sect. 3.2, using VS-IMSRG, the residual proton–neutron interaction δV_{pn} values in the upper fp shell were investigated, indicating the important role played by 3NF in explaining the experimental observations. Resonant states observed in the neutron-dripline ^{24}O and the halo structure of the known heaviest Borromean nucleus ^{22}C are presented in Sect. 3.3 for G-IMSRG. Furthermore, the low-lying resonant excited states in ^{22}C are also predicted. Section 3.4 presents the applications of the GCC method, focusing on the exotic few-body decay beyond the dripline and the intriguing phenomena in open quantum systems. Specifically, the decay dynamics and properties of exotic two-proton ($2p$) emissions are discussed, including the impact of structure, deformation, and continuum effects.

3.1 The D-IMSRG calculations of deformed light nuclei

In [53], Yuan and his collaborators developed D-IMSRG, as formulated in Sect. 2.2, which better reflects the intrinsic structure of the deformed nucleus and captures more correlations through symmetry restoration. As a test ground, the D-IMSRG was first performed to calculate the ground-state energies of ${}_{8}$Be and ${}_{10}$Be, which are exotic nuclei with 2α cluster structure or elongated shapes, benchmarked against NCSM and VS-IMSRG. Subsequently, D-IMSRG was applied to describe the ground-state properties of even–even nuclei ranging from light beryllium to medium-mass magnesium isotopes. The optimized chiral NN interaction NNLO$_{\mathrm{opt}}$ [156, 157], which gives good descriptions of nuclear binding energies, excitation spectra and neutron matter equation of state without the inclusion of the $3N$ force, was used during the calculation in [53] with $\hbar\omega = 24\,\mathrm{MeV}$.

The ground-state energies of ^{8}Be and ^{10}Be were first studied though D-IMSRG, as shown in Fig. 4, with and without the approximate angular momentum projection. It was found out that the trend of calculated energy by D-IMSRG is similar to those of NCSM [16, 84–87] and multi-reference IMSRG [19] calculations, exhibiting an exponential convergence with respect to the basis-space size N_{shell}. The energies extrapolated to infinite model space using an exponential fit based on Eq. (22)

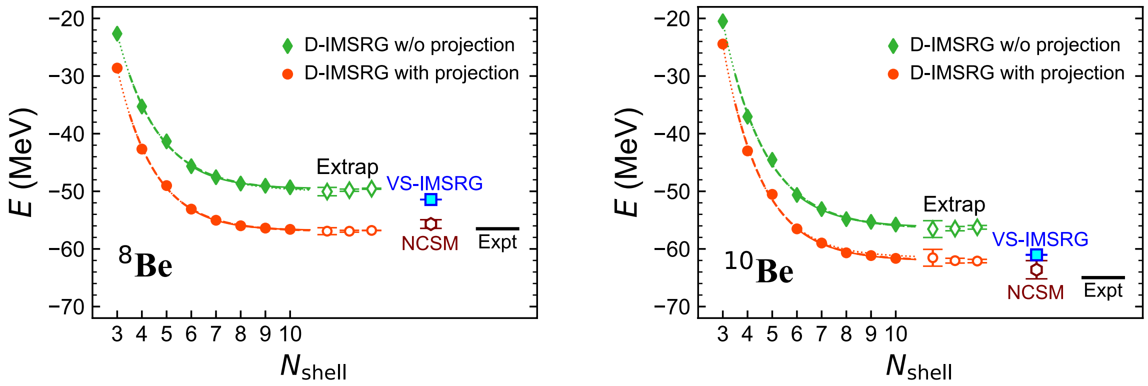

Fig. 4 (Color online) Ground-state energies for ^{8}Be and ^{10}Be calculated by D-IMSRG, with and without projection correction, are shown as a function of basis-space size $N_{\rm shell}$. Symbols below "Extrap" represent the energies extrapolated to the infinite basis space using an exponential fit, based on different data points: $N_{\rm shell}$ = 3–7, 3–10, and 6–10. The fitting uncertainties are indicated by error bars. Extrapolation uncertainties in NCSM and VS-IMSRG calculations are also represented by error bars. Experimental data were taken from AME2020 [155], and the figure was taken from [53]

are depicted in Fig. 4. The extrapolated "Extrap" results fitted with different data points are provided in Fig. 4 along with their uncertainties, verifying that the calculation results of D-IMSRG converge exponentially with an increase in $N_{\rm shell}$, thereby demonstrating the reliability of the calculations.

In Fig. 4, the angular momentum projection corrections are −7.2 MeV and −5.9 MeV for ^{8}Be and ^{10}Be, respectively. These significant corrections are caused by the large deformations of these two nuclei. The results of NCSM and VS-IMSRG and the experimental data are also shown in Fig. 4.

The results of VS-IMSRG underestimate the ground-state energy in ^{8,10}Be, which may be attributed to the omission of higher-order collective excitations that are not handled well in VS-IMSRG at the IMSRG(2) level, as discussed in [158, 159]. However, this omission can be compensated by the angular momentum projection correction through D-IMSRG, as illustrated in Fig. 4.

The ground-state energies and two-neutron separation energies calculated by D-IMSRG for $^{6-16}$Be are shown in Fig. 5 (top panel and bottom panel, respectively), along with VS-IMSRG calculations and experimental data. The angular momentum projection lowered the ground-state energies of $^{8-16}$Be by about 5–6 MeV, making the calculated energies closer to the data. Both D-IMSRG and VS-IMSRG calculations indicated that the neutron dripline of beryllium isotopes was at ^{12}Be, contrary to the experimental position of ^{14}Be, which may be due to the absence of a continuum effect [57, 105, 107, 160].

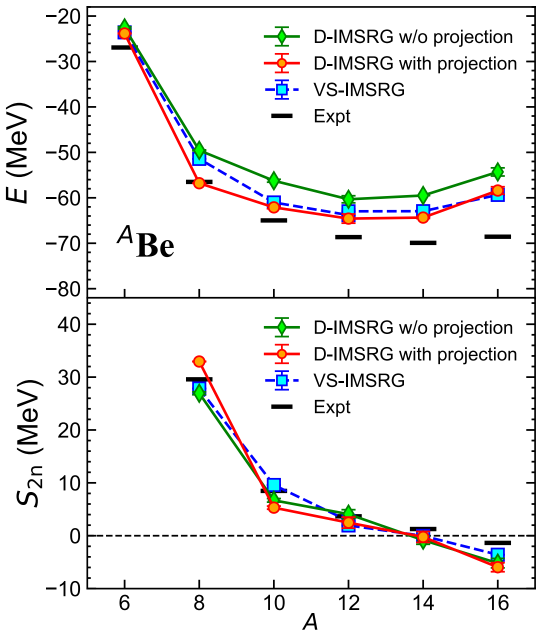

Fig. 5 (Color online) Ground-state energies (upper panel) and two-neutron separation energies S_{2n} (lower panel) of $^{6-16}$Be calculated by D-IMSRG with and without projection correction. The VS-IMSRG results and experimental data [155] are also presented for comparison. The figure is taken from [53]

In [53], the heavier nuclei of C, O, Ne, and Mg isotopes were also calculated by D-IMSRG, as shown in Fig. 6 along with VS-IMSRG calculations and experimental data. The D-IMSRG calculations with the projection correction agreed well with VS-IMSRG results and experimental data. The angular momentum projection corrections were zero for the closed-shell nuclei ^{14}C and ^{14,16,22,24,28}O, indicating the spherical characteristics of these nuclei. However, for the expected closed-shell nuclei of ^{12,22}C, the angular momentum projection corrections were not zero but −5.5 MeV and −2.7 MeV, respectively, indicating their deformation. For Ne and Mg isotopes, the projection results provided energy gains of about 3–6 MeV near the neutron number $N = 20$ island of inversion [161, 162].

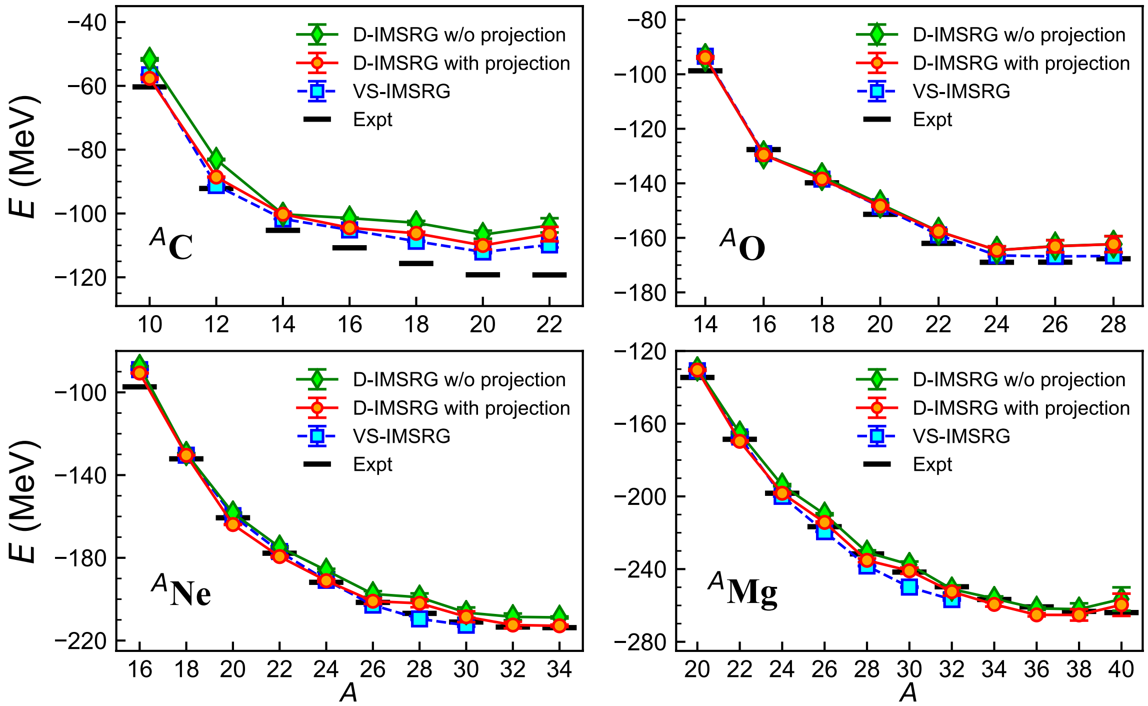

Fig. 6 (Color online) Ground-state energies of C, O, Ne, and Mg isotopes. D-IMSRG results are extrapolated to the infinite basis space using the $N_{\text{shell}} = 6{-}10$ data points, whereas the VS-IMSRG results are extrapolated based on $N_{\text{shell}} = 8{-}13$. In VS-IMSRG calculations, the model space includes both protons and neutrons in $0p_{3/2,1/2}$ for $^{6-14}$C; protons in $0p_{3/2,1/2}$ and neutrons in $1s_{1/2}0d_{5/2,3/2}$ for $^{14-22}$C; and both protons and neutrons in $1s_{1/2}0d_{5/2,3/2}$ for O, Ne, and Mg isotopes. The experimental data were taken from AME2020 [155]. The figure was taken from [53]

There is strong configuration mixing between *sd* and *pf* shells in nuclei located in the region of the island of inversion. This cross-shell mixing is missing in the VS-IMSRG calculations although a multi-shell VS-IMSRG has been proposed [163]. Therefore, it can be concluded that deformation effectively brings the deformation orbitals into the wave function of the state in D-IMSRG calculations.

For nuclei, another important observable is the charge radius. The radii of the studied isotopes were also calculated in [53]. Compared with the calculation of the ground-state energy, the convergence of the radius calculation showed a different trend with increasing basis-space size, as discussed in [32, 87, 168] and as also observed in the D-IMSRG calculations [53], indicating that the exponential fit was not applicable to the radius. Therefore, the authors in [53] did not use extrapolation to fit the radius in the calculations. The angular momentum projection correction was also estimated by the HF wave function in the study. As shown in Fig. 7, the charge radii of Be, C, O, Ne, and Mg isotopes were investigated, along with the VS-IMSRG calculations and experimental data. The projection correction to the charge radius is small, making the D-IMSRG radii with and without the projection correction close to each other and in good agreement with the VS-IMSRG calculations except for ^{8}Be, where the D-IMSRG radius is larger. This difference can be attributed to the large deformation of ^{8}Be. Therefore, it can be concluded that the calculated charge radii by D-IMSRG and VS-IMSRG are reasonable compared with experiment data, as shown in Fig. 7 although the NNLO$_{\text{opt}}$ interaction tends to underestimate the nuclear radii, as noted in [157].

3.2 δV_{pn} bifurcation by the VS-IMSRG

The VS-IMSRG was first introduced by Tsukiyama et al. in 2012 [39]. This method combines the SM and IMSRG to non-perturbatively derive effective valence-space Hamiltonians and operators, as detailed in Sect. 3.2. Recently, it has been applied to describe the δV_{pn} values in the upper *fp* shell, incorporating a chiral three-nucleon force (3NF), as reported in [169].

Nuclear binding energy $B(Z, N)$ represents the total interaction energy of interacting nucleons in the nucleus with Z protons and N neutrons. Differences in binding energy can isolate specific types of interactions and provide insights into modifications in nuclear structure [170, 171]. The double binding energy difference denoted as δV_{pn}, has been used as an important mass filter to extract the residual proton–neutron (pn) interaction [172–174], particularly for the $N = Z$

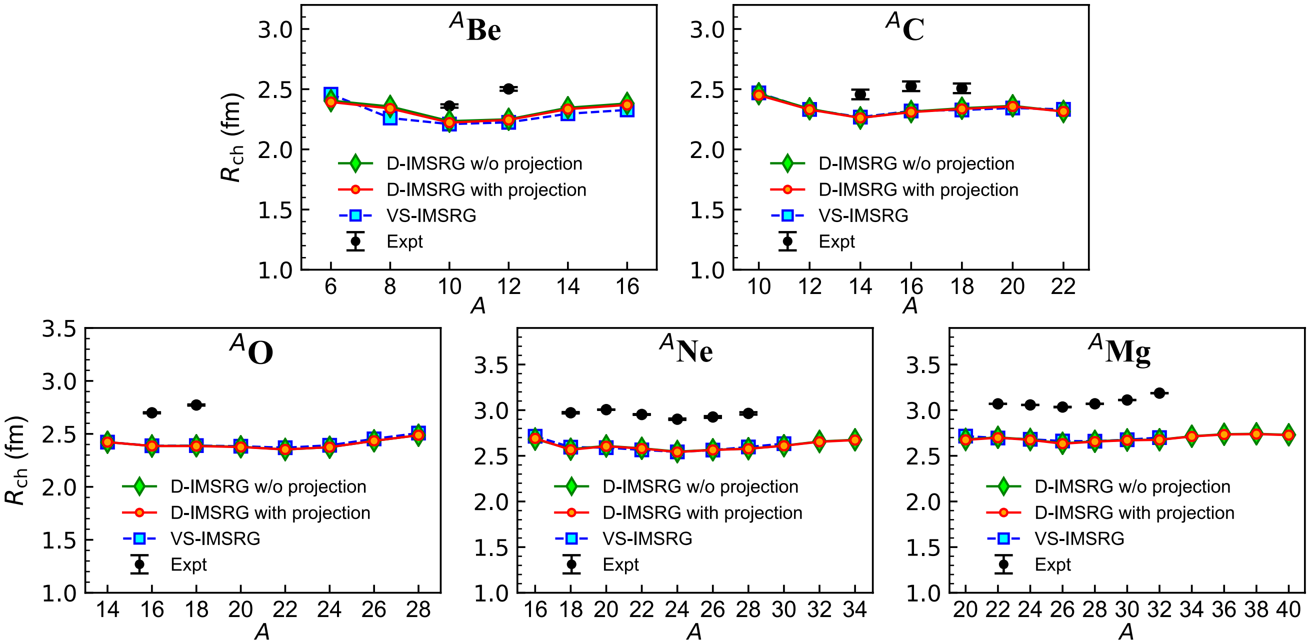

Fig. 7 (Color online) Charge radii calculated by D-IMSRG in a basis space with $N_{\mathrm{shell}} = 10$ and using VS-IMSRG with $N_{\mathrm{shell}} = 13$ for Be, C, O, Ne, and Mg isotopes. Experimental data were taken from [157, 164–167]. The figure was taken from [53]

nuclei. The residual proton–neutron interaction δV_{pn} can be extracted using

$$\delta V^{\mathrm{ee}}_{\mathrm{pn}}(Z,N) = \frac{1}{4}[B(Z,N) - B(Z,N-2) - B(Z-2,N) + B(Z-2,N-2)], \tag{58}$$

for the nucleus with $N = Z =$ an even number, and

$$\delta V^{\mathrm{oo}}_{\mathrm{pn}}(Z,N) = [B(Z,N) - B(Z,N-1) - B(Z-1,N) + B(Z-1,N-1)], \tag{59}$$

for the nucleus with $N = Z =$ an odd number.

Weakly bound proton-rich nuclei are attracting interest in novel structure [175]. In [169], the masses of ^{62}Ge, ^{64}As, ^{66}Se, and ^{70}Kr were measured for the first time. Additionally, the masses of six $N = Z - 1$ nuclides ^{61}Ga, ^{63}Ge, ^{65}As, ^{67}Se, ^{71}Kr, and ^{75}Sr were redetermined with improved accuracy, using a novel method of isochronous mass spectrometry conducted at the Heavy Ion Research Facility in Lanzhou (HIRFL). These newly measured masses provide updated δV_{pn} values, which offer great test ground for state-of-the-art theoretical calculations. The updated δV_{pn} values show a clear increasing trend in $\delta V^{\mathrm{oo}}_{\mathrm{pn}}$ beyond $Z = 28$, which is interpreted as an indication of the restoration of pseudo-SU(4) symmetry in the *fp* shell, as suggested in [176, 177]. In contrast, $\delta V^{\mathrm{ee}}_{\mathrm{pn}}$ shows a decreasing trend that was previously observed in the lower mass region [173, 178]. These δV_{pn} values were extracted using predicted masses from frequently used mass models; however, none of these models successfully reproduce the bifurcation in δV_{pn} values [169], except for the ab initio VS-IMSRG calculations. Within the ab initio VS-IMSRG calculation, a chiral 2NF plus 3NF, labeled by EM1.8/2.0 [24], is adopted, which can reproduce well the ground-state energies up to $A \approx 100$ region

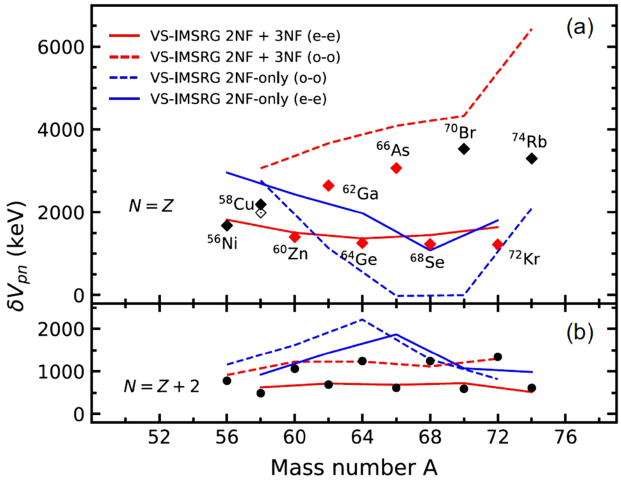

Fig. 8 (Color online) Experimental δV_{pn} for **a** $N = Z$ and **b** $N = Z + 2$ nuclei beyond $A = 56$, compared with the ab initio VS-IMSRG calculations. Data uncertainties are indicated by the size of symbols. δV_{pn} values from ab initio calculations using 2NF + 3NF and only 2NF plotted as red and blue lines (solid lines for even–even and dashed lines for odd–odd), respectively. The figure is taken from [169]

nuclei [7, 28, 179]. The effective Hamiltonian in the full *fp*-shell above the ^{40}Ca core was derived using the VS-IMSRG, and the final diagonalization of the valence-space Hamiltonian was realized using KSHELL [95].

As shown in the lower panel of Fig. 8, VS-IMSRG calculations with chiral 2NF plus 3NF reproduce the experimental δV_{pn} for the $N = Z + 2$ nuclei exceptionally well. For the odd–odd $N = Z$ nuclei, ^{62}Ga,^{66} As,^{70} Br and ^{74}Rb, the ground states have been identified as $(T, J^{\pi}) = \left(1, 0^{+}\right)$ [155]. VS-IMSRG calculations, which inherently incorporate both $T = 0$ and $T = 1$ pn correlations, achieve a commendable match with the experimental $\delta V_{\text{pn}}^{\text{oo}}$ values for nuclei ranging from ^{58}Cu to ^{70}Br. Particularly noteworthy is that the calculation successfully reproduces the observed increasing trend in $\delta V_{\text{pn}}^{\text{oo}}$ with an increase in nucleon number A. Our calculations consistently attributed an isospin of $T = 1$ to the ground states of these odd–odd nuclei, aligning with experimental results, with the exception of ^{58}Cu. Moreover, the decreased trend in the even–even $\delta V_{\text{pn}}^{\text{ee}}$ was also well reproduced by our VS-IMSRG calculations.

In mass regions with extremely asymmetric *N*/*Z* ratios, 3NF usually provides a repulsive effect on the neutron–neutron (*nn*) and proton–proton (*pp*) interactions [28, 180], which is essential for the emergence of new magic numbers [180] and also for reproducing the neutron or proton dripline [28]. To understand the role played by 3NF in the δV_{pn} of upper *fp*-shell nuclei, we performed calculations using only a chiral 2NF at N3LO. The results using only 2NF show significant deviations from those calculated with 3NF included, as demonstrated in Fig. 8. Specifically, the agreement with experimental δV_{pn} values was markedly poor in the calculations without the 3NF included. Additionally, the predicted isospins of ground states for odd–odd nuclei ranging from ^{62}Ga to ^{74}Rb were all erroneously identified as $T = 0$ in the calculations with the 3NF included, contradicting experimental data. Furthermore, without the inclusion of 3NF, the calculated $\delta V_{\text{pn}}^{\text{oo}}$ values of $N = Z$ nuclei were lower than $\delta V_{\text{pn}}^{\text{ee}}$ calculated with 3NF included. The 3NF enhances the *pn* correlations in $N = Z$ nuclei favoring a $T = 1$ isospin coupling, which changes the δV_{pn} behavior.

3.3 The G-IMSRG with the coupling to the continuum

A novel G-IMSRG [57] was developed by Hu et al., using the complex-energy Berggren representation, as introduced in Sect. 2.4. This advanced G-IMSRG is capable of describing the weakly bound and unbound nature of nuclei in the vicinity of nuclear driplines. We applied G-IMSRG to oxygen and carbon isotopes. Recent experiments [181–184] highlight that ^{22}C is a Borromean halo nucleus, with an experimentally deduced root-mean-squared matter radius of 3.44 ± 0.08 fm [184]. The continuum coupling plays a vital role in generating the extended density distribution. Notably, experimental information about the excited states of ^{22}C, which can offer additional insights into its halo structure, is lacking. In this study, we performed an ab initio G-IMSRG calculation of the halo ^{22}C, using both chiral 2NF NNLO$_{\text{opt}}$ and 2NF plus 3NF NNLO$_{\text{sat}}$ interactions. The NNLO$_{\text{opt}}$ interaction matrix elements were expanded within 12 major HO shells at a frequency of $\hbar\omega = 20$ MeV, whereas the NNLO$_{\text{sat}}$ interaction was truncated at 13 major HO shells with $\hbar\omega = 22$ MeV [158, 185]. The NNLO$_{\text{opt}}$ potential provides a good description of nuclear structure, including binding energies, excitation spectrum, and dripline position without the need for 3NF [156]. The NNLO$_{\text{sat}}$ interaction can provide accurate descriptions of charge radii in light- and mid-mass isotopes [186].

For the *sd* shell, the neutron $0d_{3/2}$ is a narrow-resonance orbital. With no centrifugal barrier of the $l = 0$ *s* partial wave, a weakly bound $1s_{1/2}$ orbital can significantly affect the spatial distribution of the wave functions of weakly bound nuclei. Therefore, the $0d_{3/2}$ and $1s_{1/2}$ orbitals should be treated in the Berggren basis, which includes coupling to the continuum, whereas other orbitals can be treated in the real-energy HF basis to reduce the computational cost, as in [57].

Although the Hamiltonian (5) is intrinsic, the IMSRG wave functions are expressed in laboratory coordinates. Therefore, considering center-of-mass (CoM) motion corrections may be necessary. Our previous work has indicated

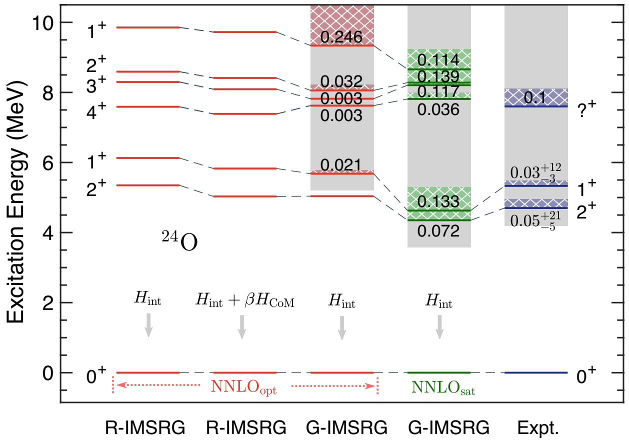

Fig. 9 (Color online) ^{24}O spectra calculated using NNLO$_{\text{opt}}$ and NNLO$_{\text{sat}}$ interactions. The first two columns display the results from real-energy EOM-IMSRG calculations (denoted as R-IMSRG) without and with CoM treatment βH_{CoM}, using the multiplier $\beta = 5$. The subsequent three columns present the EOM-G-IMSRG calculation (denoted as G-IMSRG), which are compared with the data from [188, 189]. Resonant states are highlighted by shading, and their widths (in MeV) are annotated nearby. The gray shading indicates the continuum region above the particle emission threshold. The figure is taken from [57]

that the CoM effect on an intrinsic Hamiltonian is small for low-lying states [105]. Thus, the approximation method suggested in [37, 187] can be adopted to estimate the CoM effect in IMSRG calculations. Figure 9 presents real-energy EOM-IMSRG calculations without and with the CoM multiplication term $\beta H_{\mathrm{CoM}} = \beta\left(\frac{\boldsymbol{P}^2}{2mA} + \frac{1}{2}mA\tilde{\omega}^2\boldsymbol{R}^2 - \frac{3}{2}\hbar\tilde{\omega}\right)$. Note that the value of the CoM vibration frequency $\tilde{\omega}$ can differ from the ω frequency of the HO basis [187]. As illustrated in Fig. 9, the CoM effect remains negligible for these low-lying states.

As described in Sect. 2.4, the equation-of-motion approach can be used to calculate nuclear excited states. Figure 9 presents the calculated spectrum of ^{24}O, showing resonant excited states. The EOM Gamow IMSRG (indicated by EOM-G-IMSRG) calculations reproduced the experimental excitation energies and resonance widths of the observed states well. A high excitation energy of the first 2^+ state supports the shell closure at $N = 16$ in the oxygen chain. Additionally, the calculation predicted three resonant states around the excitation energies of 8 MeV with $J^\pi = 2^+ - 4^+$, aligning with the experimentally ambiguous states observed around 7.6 MeV [189]. This finding is consistent with the complex coupled cluster calculation which uses a schematic 3NF [18].

The Borromean halo nucleus ^{22}C poses significant challenges for many theoretical models [58–60]. Our GHF calculations suggested that the neutron $\nu 1s_{1/2}$ orbital is weakly bound. Therefore, the two-neutron configuration $(\nu 1s_{1/2})^2$ is responsible for the formation of the halo structure [181–184]. Figure 10 presents the ground-state densities of ^{22}C calculated by the real-energy R-IMSRG and complex-energy G-IMSRG using two different chiral interactions. The density was computed by an effective density operator evolving within the Magnus framework (16, 17). The G-IMSRG calculation revealed a long tail in the density distribution, supporting the halo structure of ^{22}C.

To assess the continuum effect of the s channel on the properties of ^{22}C, we performed two types of G-IMSRG calculations using: (i) discrete s states obtained from the real-energy HF calculation, and (ii) Berggren s states obtained from the complex-energy GHF calculation. In both calculations, the neutron $d_{3/2}$ channel remained in the GHF basis. Calculations using NNLO$_{\mathrm{opt}}$ with discrete real-energy HF s states yielded a radius of 2.798 fm for the ^{22}C ground state, which increased to 2.928 fm upon incorporating the continuum s wave. Similarly, the calculations using NNLO$_{\mathrm{sat}}$ yielded a radius of 2.983 fm for the real-energy discrete s states and 3.139 fm for the continuum GHF s wave. The experimentally estimated radius was reported to be 5.4 ± 0.9 fm in an earlier work [181], and later works found it to be 3.44 ± 0.08 fm [184] and 3.38 ± 0.10 fm [190]. These findings highlight the crucial role of the continuum s wave in predicting the radius and understanding the halo structure.

Currently, no experimental data are available for the excited states in ^{22}C. Figure 11 displays the EOM-G-IMSRG predictions of low-lying states, benchmarked against results from complex CC calculations. Both methods yielded consistent results. The first 2^+ excited state was bound in both G-IMSRG and coupled cluster calculations. We found that the 2_1^+ state was dominated by the proton $1p1h$ excitation from the proton $0p3/2$ hole to proton $0p1/2$ particle orbits. The proton 2_1^+ excited state was lower in energy than the neutron 2^+ state calculated by the real-energy SM with the

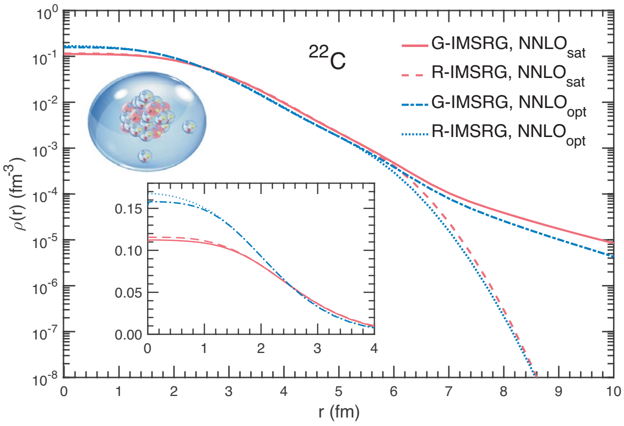

Fig. 10 ^{22}C ground-state densities calculated by real-energy IMSRG (R-IMSRG) and Gamow IMSRG (G-IMSRG), displayed on a logarithmic scale. The inset provides a detailed view of the densities in the central region of the nucleus on a standard scale. The figure is taken from [57]

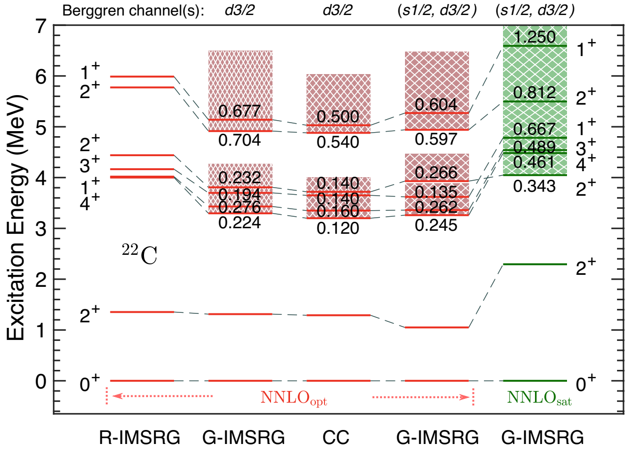

Fig. 11 Excited states in ^{22}C predicted by R-IMSRG and G-IMSRG using two different chiral interactions compared with complex coupled cluster results. The channels listed at the top of the panel indicate that the partial waves are treated in the resonance and continuum Berggren representation. The other labels are the same as those in Fig. 9. The figure is taken from [57]

^{14}C core [191, 192]. The real-energy R-IMSRG results in Fig. 11 show a neutron 2^+ energy similar to that in [191, 192]. Additionally, there were superposed resonant states with $J^\pi = 1^+ - 4^+$ at energies of 3.5–4.0 MeV and widths of $0.15 - 0.25$ MeV. The NNLO$_{\text{sat}}$ calculations yielded slightly higher excitation energies and broader resonant widths for these states, as illustrated in Fig. 11. The resonances were primarily characterized by neutron $1p1h$ excitations from the $\nu 0d_{5/2}$ hole to $\nu 0d_{3/2}$ particle orbitals. Structure and decay modes of loosely bound nuclei are of interest in many respects [193, 194].

3.4 Few-body decay by GCC

In this section, the discussion centers on the decay properties of open quantum systems, with a particular focus on two-proton ($2p$) emitters, exploring how deformation and continuum effects influence the decay dynamics of these systems. Previous research highlighted the significant role that these factors play in shaping the decay characteristics of $2p$ emitters. A critical aspect of our analysis involves extracting structural information from these systems through the measurement of asymptotic nucleon–nucleon correlations, which are experimentally accessible.

In analyzing these correlations, the objective is to deepen our understanding of the universal properties inherent to open quantum systems. This approach not only elucidates the fundamental interactions within these systems but also provides a framework for interpreting experimental results in terms of underlying nuclear structure and dynamics. Such insights are invaluable for advancing our comprehension of the complex behaviors exhibited by open quantum systems under various conditions.

3.4.1 Impact of structure on the decay process

As the heaviest $2p$ emitter identified to date, ^{67}Kr serves as a pivotal case study for examining the influence of structure on decay properties. Notably, shape coexistence is often observed with Kr isotopes. In addition, the deformation effects can significantly impact the lifetime of a decaying system, as evidenced by prior research on one-proton ($1p$) emitters [135–137, 144, 195–199]. This offers a good opportunity to study how the $2p$ decay properties change as a function of deformation.

As discussed in [68], Fig. 12a illustrates the proton Nilsson levels (labeled by asymptotic quantum numbers $\Omega[\mathrm{N}n_z\Lambda]$) within the core-$p$ potential. At modest deformations, specifically $|\beta_2| \leq 0.1$, the valence protons predominantly occupy the $f_{5/2}$ shell. The half-life predicted under vibrational conditions, calculated as $T_{1/2} > 218$ ms, significantly surpasses the experimentally observed value by more than an order of magnitude, as depicted in Fig. 12b. This discrepancy underscores the need for further theoretical refinement and is consistent with prior theoretical estimates [200, 201], suggesting an intricate interplay between nuclear structure and decay dynamics in ^{67}Kr.

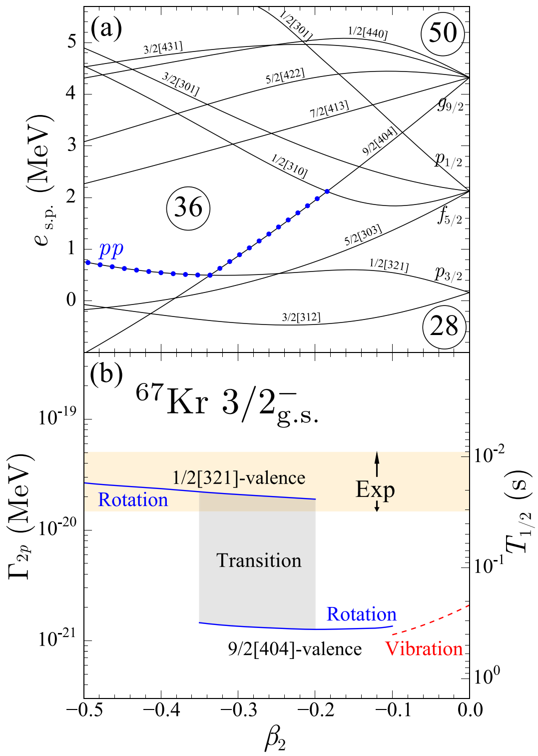

Fig. 12 Top: Nilsson levels $\Omega[\mathrm{N}n_z\Lambda]$ of the deformed core-p potential as a function of the oblate quadrupole deformation β_2 of the core. The dotted line indicates the valence level primarily occupied by the two valence protons. Bottom: Decay width (half-life) of the $2p$ ground state radioactivity of ^{67}Kr. The solid and dashed lines mark the results for the rotational and vibrational couplings, respectively. The rotational-coupling calculations were carried out by assuming that the 1/2[321] orbital is either occupied by the core (9/2[404]-valence) or valence (1/2[321]-valence) protons. The figure is taken from [68]

As the core deformation increases, a notable oblate gap at $Z = 36$ emerges due to the descending 9/2[404] Nilsson level, which stems from the $0g_{9/2}$ shell. This gap plays a crucial role in shaping the oblate ground state (g.s.) configurations of proton-deficient Kr isotopes [202–204]. As the oblate deformation intensifies, the structure of the valence proton orbital transitions from the 9/2[404] ($\ell = 4$) state to the 1/2[321] orbital, featuring a significant $\ell = 1$ component. The precise level crossing between 1/2[321] and 9/2[404] is contingent on the specifics of the core-proton parametrization, yet the overarching pattern remains consistent as depicted in Fig. 12a: a shift from the $2p$ wave function dominated by $\ell = 4$ components toward $\ell = 1$ components as the oblate deformation progresses.

Figure 12b illustrates the predicted $2p$ decay width within the rotational model for two scenarios: (i) the 1/2[321] level is integrated into the core with the valence protons predominantly residing in the 9/2[404] level, and (ii) the valence protons primarily occupy the 1/2[321] level. Consequently, the reduction in ℓ content within the $2p$ wave function markedly enhances the decay width.

At a deformation of $\beta_2 \approx -0.3$, aligned with estimates from mirror nuclei and various theoretical models [202, 205, 205–208], the calculated $2p$ ground state half-life of ^{67}Kr is 24^{+10}_{-7} ms. This estimation not only concurs with experimental findings [209] but also underscores the significant impact of nuclear shape and structural dynamics on the decay properties of ^{67}Kr.

3.4.2 Dynamics of two-proton decay

For the light $2p$ emitters, both direct and sequential decays are possible [210, 211], providing a good opportunity to study the decay dynamics as well as the interplay between nucleon–nucleon correlation and single-particle emission.

An illustrative example is the decay of ^{6}Be, where the neighboring g.s. of ^{5}Li exists as a broad resonance, characterized by a proton decay width of $\Gamma = 1.23$ MeV [212]. The complex three-body decay dynamics of ^{6}Be remain an area of active research and debate, with existing studies indicating unresolved aspects of the decay [141, 211, 213–219]. Theoretical predictions of a diproton structure and experimental observations of broad angular correlations between emitted protons lead to conflicting interpretations.

Based on the time-dependent approach, Fig. 13a, b depicts the temporal evolution of the $2p$ density and momentum distribution in the ground state of ^{6}Be across an extensive time frame. Initially, at $t = 0$, the wave function inside the nucleus shows a localized character with a density distribution exhibiting two maxima. These maxima represent diproton (compact) and cigar-like (extended) configurations based on the relative distances between the valence protons [220].

As the decay progresses, Fig. 13b highlights two predominant flux branches. The primary branch shows protons emitted at narrow angles, indicating the presence of a diproton structure during the tunneling phase. This phenomenon is interpreted through nucleonic pairing, which favors low angular momentum states, reducing the centrifugal barrier and enhancing the $2p$ tunneling likelihood [149, 150, 216, 220]. The secondary branch illustrates protons emitted in nearly opposite directions. Despite their spatial separation, these protons exhibit simultaneous decay, suggesting three-body decay dynamics characterized by correlated decay pathways of the protons with respect to the core. This configuration reveals intricate interplays within the decay process, shedding light on the multifaceted nature of three-body decays in light $2p$ emitters.

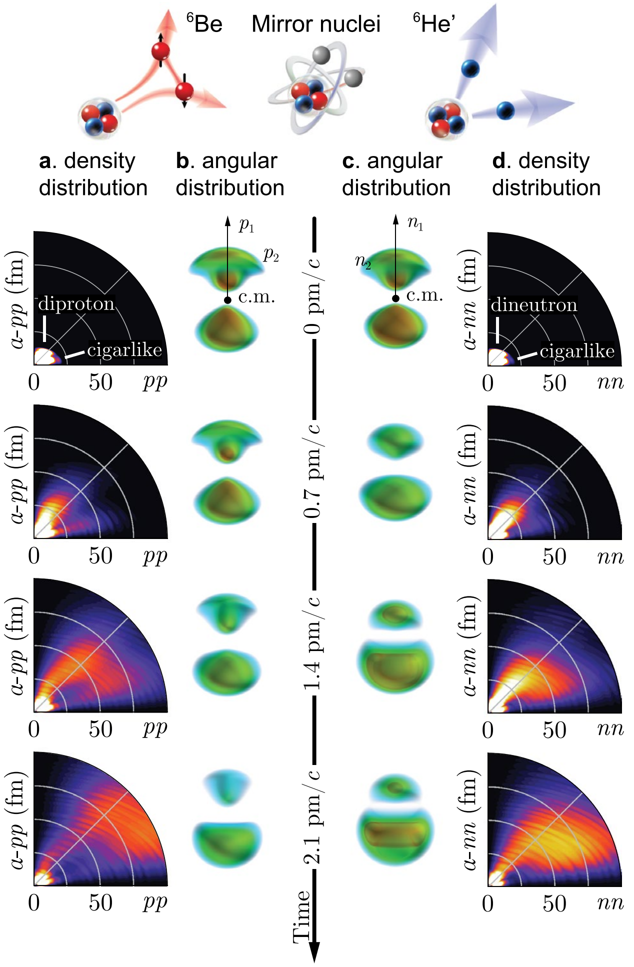

Fig. 13 The density and momentum distributions of two-nucleon decays from the g.s. of ^{6}Be (left) and ^{6}He$'$ (right) for four different time slices. The density distributions are shown in the Jacobi-T coordinates (see Fig. 3). The momentum distribution of the second nucleon is depicted with respect to the momentum of the first nucleon. To clearly show the asymptotic wave function, all the particle densities (in fm^{-1}) are multiplied by the polar Jacobi coordinate ρ. The dimensionless momentum (angular) distributions are divided by the total momentum k. The figure is taken from [70]

After tunneling through the Coulomb barrier, the two emitted protons tend to gradually separate due to Coulomb repulsion. This is reflected in the bent trajectory of the diproton decay branch and gradual reduction of the momentum alignment observed in Fig. 13a, b. Eventually, the $2p$ density becomes spatially diffuse, which is consistent with the broad angular distribution measured in [217]. One may notice that even beyond 100 fm (at $t \approx 2$ pm/c), the Coulomb repulsion tends to reduce the inter-proton correlation. According to our calculations, the angular correlation starts to stabilize only after very long times greater than 9 pm/c. Therefore, to obtain meaningful estimates of asymptotic observables, very long propagation times are required.

After the protons tunnel through the Coulomb barrier, the Coulomb repulsion between them leads to an increasing spatial separation, impacting their trajectories and momentum alignment. This dynamic is depicted in the bending trajectory of the diproton decay branch, and a reduction in momentum alignment is observed in Fig. 13a, b. Over time, the $2p$ density distribution becomes increasingly diffuse, aligning with the broad angular distributions reported in experimental studies such as [217].

To provide insights into the nuclear-Coulomb interplay in two-nucleon decay processes, an artificially unbound variant of ^{6}He, denoted as ^{6}He$'$, was built to study its two-neutron decay. Initially, the density distributions of ^{6}He$'$ and ^{6}Be display similarities, as depicted in Fig. 13, a consequence of the isospin symmetry inherent in the nuclear force.

However, the absence of Coulomb repulsion in the ^{6}He$'$ scenario significantly influences the decay dynamics. In the case of ^{6}He$'$, the dineutron decay branch is more pronounced, with the emitted neutrons maintaining their spatial correlations over time more robustly than their proton counterparts in ^{6}Be. This differential behavior leads to distinct nucleon–nucleon correlation patterns in the asymptotic regime. As a result, the nucleon–nucleon correlations observed in ^{6}He$'$, as illustrated in Fig. 14, diverge markedly from those in ^{6}Be, underscoring the critical role of Coulomb forces in shaping the decay pathways and final-state interactions in these mirror nuclei.

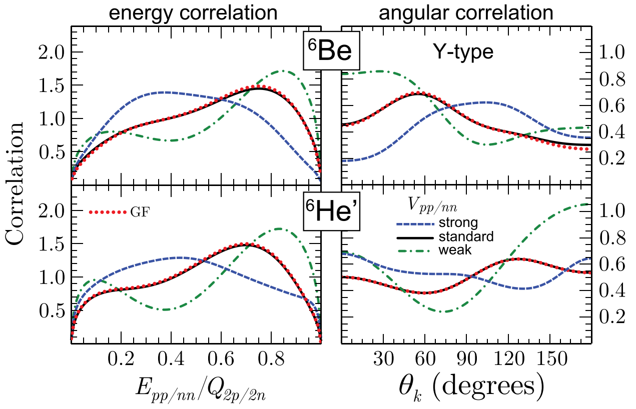

Fig. 14 Asymptotic energy (left) and angular (right) correlations of emitted nucleons from the g.s. of ^{6}Be (top) and ^{6}He$'$ (bottom) calculated at $t = 15\,\mathrm{pm}/c$ with different strengths of the Minnesota interaction [221]: standard (solid line), strong (increased by 50%; dashed line), and weak (decreased by 50%; dash-dotted line). Also shown are the benchmarking results obtained using the Green's function method (GF; dotted line) with standard interaction strength; θ_k is the opening angle between $\vec{k}_x$ and $\vec{k}_1$ in the Jacobi-Y coordinate system, and $E_{\mathrm{pp/nn}}$ is the kinetic energy of the relative motion of the emitted nucleons (see Fig. 3 for definitions). The figure is taken from [70]

3.4.3 Nucleon–nucleon correlations

The experimental measurements of nucleon–nucleon correlations among emitted nucleons provide data pertinent to the nuclear structure. This methodology serves as a distinctive avenue for investigating the internal structure and decay mechanisms of $2p$ emitters. However, the nucleon–nucleon correlations recorded by detectors are influenced by final-state interactions and distort the original nuclear correlations. Consequently, self-consistent theoretical frameworks are urgently required to establish a linkage between the nuclear structure and observed asymptotic correlations. In this section, we elucidate how the GCC method and time-dependent (TD) approach have been effectively employed to address such challenges.

Compared to the neutron dripline, the proton dripline is relatively closer to the line of β-stability, facilitating the acquisition of $2p$ correlation data in several instances, as evidenced by the findings reported in studies [222, 223]. Remarkably, the energy correlation of protons emitted from the ground state of ^{12}O closely resembles those observed in other *sd*-shell $2p$ emitters, such as ^{16}Ne and ^{19}Mg. This resemblance suggests potential structural similarities in the configurations of valence protons across these isotopes despite their differing proton numbers. This observation underscores the intricate interplay between nuclear structure and decay processes, hinting at underlying uniformities in the spatial and energetic distributions of valence protons within this specific shell.

To elucidate the $2p$ correlation patterns observed in ^{12}O and its isotonic neighbor ^{11}O, a time-dependent approach was employed, as detailed in recent research [71]. The initial $2p$ density configurations in ^{11,12}O exhibit a prominent diproton arrangement alongside a secondary, cigar-like structure [220, 224], bearing resemblance to configurations typical of p-shell nuclei. However, in the case of ^{12}O, the protons emerging from these configurations coalesce, leading to a broad distribution as reported in [71]. This pattern contrasts starkly with the decay dynamics of ^{6}Be, as shown in Fig. 13 and [70]. These observations align with the flux current calculations presented in [220], which indicate a competitive interplay between diproton and cigar-like decay modes, culminating in a so-called democratic decay process. This comparative analysis underscores the complex interdependencies within nuclear decay pathways and highlights the distinctive decay characteristics of ^{12}O relative to its nuclear peers.

Consequently, the asymptotic $2p$ correlations for ^{12}O, as depicted in Fig. 15, demonstrate robust alignment with the empirical data [223] and corroborate prior theoretical investigations [225]. Notably, the subtle discrepancies between the experimental results and theoretical predictions, enhanced via Monte Carlo simulations incorporating

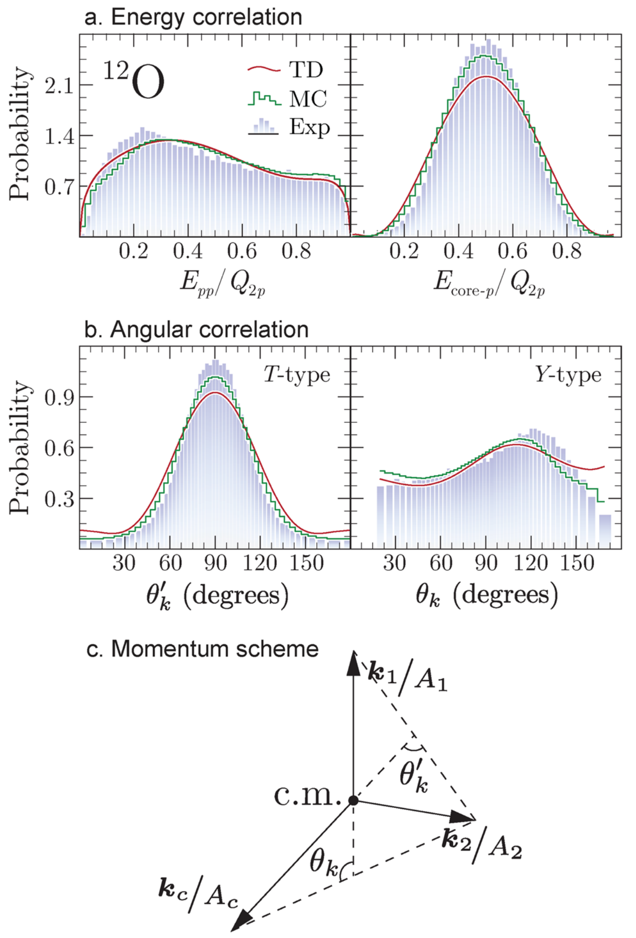

Fig. 15 Asymptotic **a** energy and **b** angular correlations of the protons emitted from the two-proton unbound ^{12}O isotope. Also shown is **c** the momentum scheme for three-body system. Theoretical distributions were obtained within the time-dependent approach (TD, red line) at $t = 15\,\text{pm}/c$. MC (green line chart) labels the Monte Carlo simulation of TD results which include experimental resolution and efficiency [223]. The calculated $2p$ correlations (TD and MC) are compared with experimental data (Exp, blue histogram) of [223]. A is the mass number and k_1, k_2, and k_c are the momenta of the nucleons n_1 and n_2, and the core c, respectively, in the c.m. coordinate frame. The figure is taken from [71]

experimental acceptance and resolution, might be mitigated by refining the Minnesota force initially utilized for modeling the nucleon–nucleon interactions. More importantly, the absence of distinct diproton emissions during the temporal evolution suggests that a low-E_{pp} correlation does not inherently imply a diproton decay. Moreover, recognizing that the $2p$ system may manifest as a subthreshold resonance characterized by a broad decay width around 1 MeV [226], is critical. This continuum characteristic potentially influences the energy correlation observed in $2p$ emitters possessing minimal decay energies, underscoring the complex interplay between nuclear structure and decay dynamics.

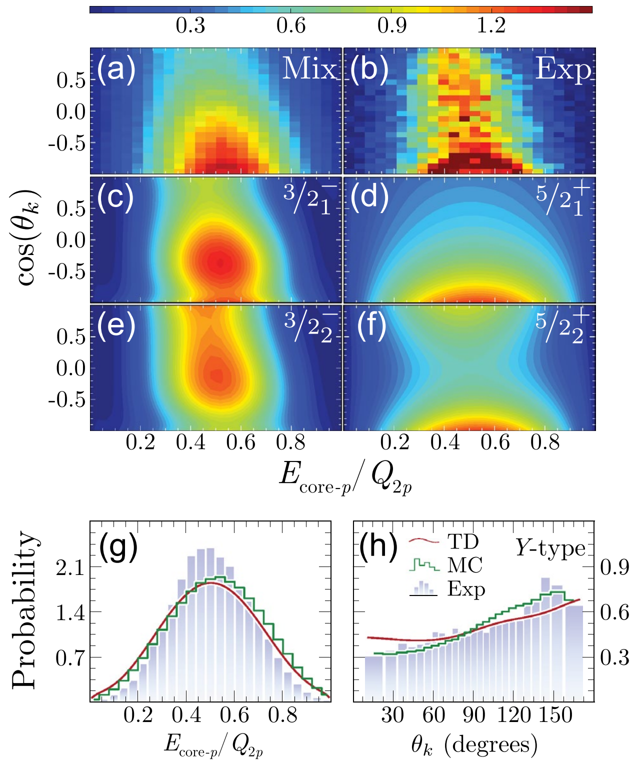

Fig. 16 **a** Theoretical and **b** experimental Jacobi-Y correlations of the two protons emitted from the broad low-energy structure in ^{11}O; **c**–**f** the corresponding contributions predicted from each low-lying state. The experimental resolution and efficiency have been considered in (**a**) Monte Carlo simulations. Also shown are the corresponding **g** energy and **h** angular correlations obtained in the time-dependent (TD) calculations (red line), Monte Carlo (MC) simulations (green step chart), and experiments (Exp, blue histogram). The figure is taken from [71]

To further illustrate, the lightest oxygen isotope, ^{11}O, has been characterized as a broad structure encompassing multiple resonances [224, 227–230]. Utilizing GCC calculations, four low-lying states with quantum numbers $J^\pi = 3/2_1^-$, $5/2_1^+$, $3/2_2^-$, and $5/2_2^+$ were predicted within the experimental energy range [220]. Each state exhibits a substantial decay width ranging from 1 MeV to 2 MeV. In the time-dependent calculations [71], these states were propagated individually, effectively disregarding potential interference effects. This approach underscores their significant decay widths, which foster robust continuum coupling, resulting in a more homogeneous density distribution throughout the decay process compared to ^{12}O, as noted in [71].

The emergent Y-type correlations exhibit a pronounced dependency on angular momentum, which can be instrumental in experimentally determining spin assignments. To simulate the asymptotic correlations of the emitted valence protons, the correlations of these four states were amalgamated, utilizing the weights derived from resonance-shape fitting [224]. This composite correlation, depicted in Fig. 16a, closely aligns with the experimental observations shown in Fig. 16b, lending credence to the hypothesis that the observed broad structure integrates states with $J^{\pi} = 3/2^-$ and $5/2^+$ [224, 227]. Moreover, Fig. 16g, h illustrates the energy and angular correlations, respectively, adjusted for experimental resolution and efficiency. The qualitative agreement between these corrected simulations and experimental data provides additional support for the multi-resonance composition within the observed peak, further validating the complex resonance structure of ^{11}O.

3.4.4 Exotic decays in open quantum systems

In addition to $2p$ decay, there exist several other exotic decay modes in nuclear physics, such as two-neutron decay, two-alpha decay, and multi-particle emission. These decay processes exhibit intriguing behaviors that are unique to the quantum realm. The classical understanding of radioactive decay is based on the principle that the rate of decay is directly proportional to the quantity of the radioactive substance present. This model fundamentally assumes that the decay is a stochastic process at the level of individual particles, meaning that the probability of decay is independent of the system's previous history.

However, this classical perspective is challenged within the quantum framework due to phenomena such as memory effects and quantum entanglement. These effects introduce deviations from the exponential decay law, traditionally used to describe radioactive decay. Notably, quantum mechanics reveals that decay probabilities can exhibit non-exponential behavior at very short and very long timescales. Theoretical and experimental studies have demonstrated that quantum systems do not always follow the expected exponential decay pattern [151, 231–241].

These findings underscore the complex nature of decay processes in quantum systems, where the inherent properties of the particles and their interactions can lead to observable departures from classical predictions. The implications of these quantum behaviors are profound, impacting our understanding of fundamental decay processes and the predictive models used in nuclear physics.

In analyzing the non-exponential decay in quantum systems, one crucial concept is the survival amplitude $\mathcal{A}(t)$. This amplitude is defined as the overlap between the initial quantum state $\Psi(0)$ and the state at a later time $\Psi(t)$. Mathematically, the survival amplitude can be expressed and computed using the Fourier transform of the spectral function $\rho(E)$, as illustrated in [242]:

$$\mathcal{A}(t) = \langle \Psi(0) | \Psi(t) \rangle = \int_0^{+\infty} \rho(E) e^{-i \frac{E}{\hbar} t} \mathrm{d}E. \tag{60}$$

In this formulation, $\rho(E)$, which is the probability density of finding a system with energy E, is derived from the squared modulus of the projection of the state vector Ψ onto the real-energy eigenstates $\langle E|\Psi\rangle$. Thus, $\rho(E) = |\langle E|\Psi\rangle|^2$ represents the distribution of the initial state over the various energy eigenstates.

The survival probability $\mathcal{S}(t)$, which is a measure of the likelihood that the system remains in its initial state at time t, is then calculated in a straightforward manner from the survival amplitude:

$$\mathcal{S}(t) = |\mathcal{A}(t)|^2. \tag{61}$$

This probabilistic measure reflects how the state evolves over time, deviating from its initial configuration. This deviation is a key indicator of quantum mechanical effects in decay processes and provides insight into the complex nature of quantum dynamics.

Non-exponential decay of a threshold resonance. The survival probability of a quantum state is intrinsically linked to the energy distribution described by the spectral function of the system. Typically, for a system exhibiting exponential decay, the spectral function is expected to follow a Breit–Wigner distribution, characterized by a Lorentzian shape centered around the resonance energy with a width corresponding to the decay rate. However, this does not hold for near-threshold states, particularly those with large decay widths [151, 233, 240, 241, 243].

These near-threshold states often display significant deviations from the exponential decay law. The temporal evolution of resonance states has been shown to involve both exponential and non-exponential components [244, 245]. The exponential components, characterized by a rapid decrease in probability, dominate the early time behavior of the decay process. However, as these components decay, the non-exponential elements become more prominent.

Over time, as the influence of the exponential decay wanes, a transition to a power-law regime becomes inevitable. This regime is indicative of the long-time tail behavior common to quantum systems with broad spectral distributions. Such transitions are crucial for understanding the full dynamics of decay processes, particularly in scenarios where classical exponential decay laws fail to capture the complexities introduced by quantum mechanical principles.

Figure 17a, c illustrates this transition, highlighting how the decay initially follows an exponential decrease before transitioning to a power-law decay. This behavior underscores the complex nature of quantum decay processes and the need for a deeper exploration into the underlying

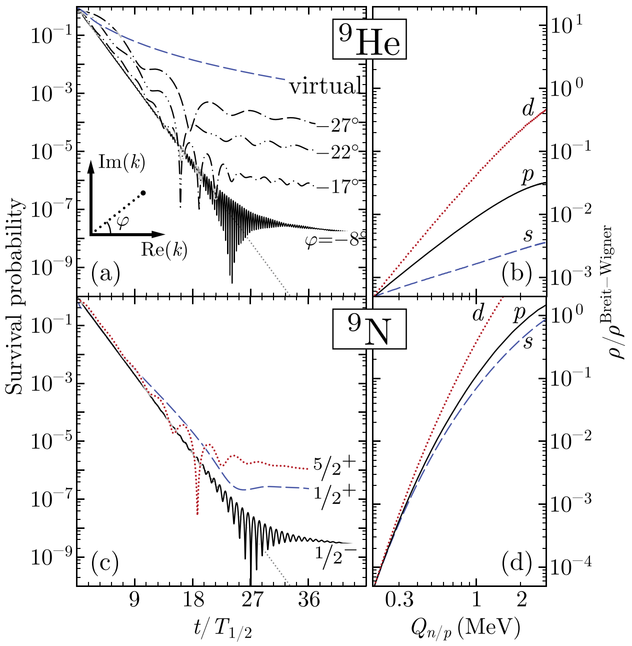

Fig. 17 Survival probability $\mathcal{S}(t)$ as a function of time (relative to $T_{1/2}$) for **a** the $1/2^-$ state of ^{9}He for different depths V_0 of the Woods–Saxon (WS) potential, and **c** the low-lying states of ^{9}N. The near-threshold behavior of the spectral function ρ (relative to the Breit–Wigner distribution) is shown for **b** neutron and **d** proton s, p, d partial waves. The polar angle φ indicates the location of the resonant state in the complex-k plane. Also shown is the survival probability for the virtual $1/2^+$ state in ^{9}He. For this state, $T_{1/2}$ was assumed to be 20 fm/c. The figure is taken from [246]

physics, particularly for states near the energy threshold or those with significant quantum mechanical interactions.

The universality of the transition from exponential to non-exponential decay is a key characteristic of quantum decay processes, the specific dynamics of which are deeply influenced by several factors. These include the structure of the initial state, the chosen decay channel, and notably, the nature of the scattering continuum which drives the post-exponential decay behavior [246].

To provide a concrete example of these dynamics, the survival probability of the $1/2^-$ resonant state in ^{9}He has been analyzed by adjusting the depth of core-nucleon potential used in the calculations [246]. This adjustment affects the resonant states, which can be characterized in the complex-k plane. The positioning of these states is determined using the polar angle $\varphi = -\cot^{-1}(2E/\Gamma)/2$, which offers insights into the relative contributions of the exponential and non-exponential decay components in state evolution.

In this analysis, as depicted in Fig. 17a, the deviations from exponential decay become increasingly pronounced as φ shifts toward −45°. This angular movement suggests a strengthening of the non-exponential decay component, particularly in threshold resonances where the resonant energy E_r is approximately equal to the decay width Γ. This result is consistent with [240, 247, 248], which indicate that post-exponential decay features tend to dominate more rapidly in systems where the resonance lies near the decay threshold. Such resonances provide a clearer and more readily observable transition to non-exponential decay, making them ideal subjects for experimental and theoretical studies aiming to explore quantum decay dynamics beyond the conventional exponential model.

Interference between near-lying states. Besides the threshold effect, the decay dynamics of quantum systems can also be significantly influenced by the interaction between closely lying resonances, particularly when these states share the same spin-parity configuration. This scenario leads to an intricate interplay due to the interference between overlapping resonances, which in turn modify the decay characteristics [249–251].

The mechanism underlying this behavior is related to the quantum interference effects, whereby the wavefunctions of the resonant states overlap and coherently interact with the continuum states. This interplay can lead to a redistribution of decay widths among the resonances, with one or more states experiencing an enhancement in decay widths due to the increased coupling [252–255]. This enhanced coupling is a critical factor in the non-exponential decay characteristics observed in such systems, as it directly impacts the decay pathways and probabilities.

To provide a detailed examination of how continuum coupling affects the spectral functions of overlapping resonances, a hypothetical study was conducted on a two-level 0^+ system in an artificial nucleus labeled as ^{6}He′ [246]. This recent study [246] explored how two 0^+ states, lying close in energy, interact with each other and the continuum, highlighting that the interference between these states not only affects their individual decay rates but also alters the overall spectral shape of the system. This interaction leads to one of the resonances showing a collective enhancement in decay width, which is a direct manifestation of the increased coupling with the continuum.

In this scenario, the excited state $|1\rangle$ predominantly features a d^2 configuration, whereas the ground state $|2\rangle$ mainly consists of a p^2 configuration. Figure 18 illustrates the evolution of the spectral functions and the corresponding survival probabilities for different energy splittings, $\Delta E = |E_r(1) - E_r(2)|$, of the doublet states.

When the energy splitting ΔE is large, only a minor suppression occurs at the tail of the spectral function for state $|2\rangle$, and both states exhibit comparable decay widths. However, as the states begin to overlap, significant interference effects arise, which dramatically impact the spectral functions of the doublet (Fig. 18e, f). This interference leads to

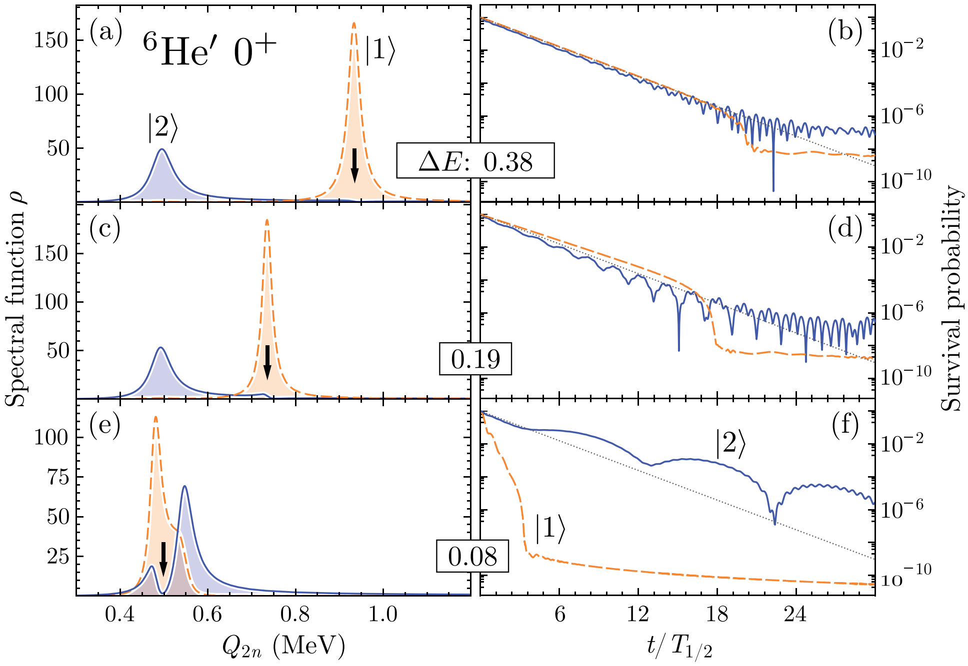

Fig. 18 Interference between two close-lying 0^+ resonances in ^{6}He′ for the three values of the doublet ΔE (in MeV) energy splitting. Left: Spectral functions versus decay energy. The arrow indicates the suppression of the spectral function of |2⟩. Right: Time dependence of the corresponding survival probabilities. The decay widths (in keV) of the doublet (Γ_1, Γ_2) are (34, 60), (30, 52), and (6, 68) for large, moderate, and small values of ΔE, respectively. The figure is taken from [246]

pronounced deviations from the exponential decay regime in survival probabilities.

Specifically, state |1⟩ decays much more rapidly than its intrinsic decay width would suggest, whereas state |2⟩ exhibits a remarkably slow decay. These observations are consistent with the findings of previous studies [253, 255], which discuss how such exponential deviations during the decay process can occur between any near-lying resonances of the same spin-parity. This phenomenon is driven by virtual transitions governed by the scattering continuum and differing orbital angular momentum structures of the doublet states.

This behavior highlights the complex dynamics that can arise from interference effects in quantum decay processes, particularly when closely spaced resonances are involved. The interplay between the initial state configurations, decay channels, and the nature of the continuum coupling leads to non-trivial modifications in decay rates and survival probabilities, underscoring the intricate nature of quantum mechanical decay processes.

4 Summary

In this paper, recent developments in IMSRG were reviewed, focusing on our work on deformed IMSRG and Gamow IMSRG. The developed IMSRG approaches were successfully applied to nuclei which are elongated in shape or exhibit weakly bound or even unbound resonance. The reaction-related GCC method and its extensions to deformed systems and time-dependent approaches are also summarized. Starting with the axially deformed HF reference state, the D-IMSRG enables the IMSRG to compute open-shell nuclei and includes important deformed configurations. The valence-space IMSRG was first developed by Tsukiyama et al. to derive an ab initio shell-model effective interaction in a non-perturbative way. We used this method to investigate the residual neutron–proton interaction δV_{pn} in the upper *fp* shell with chiral 3NF included. The bifurcation of even–even and odd–odd δV_{pn} values were found experimentally in this region.

Without 3NF, we could not reproduce the bifurcation in this region, which in turn means that 3NF plays a vital role on the behavior of δV_{pn} by enhancing the *pn* correlations with a stronger $T = 1$ isospin coupling. The G-IMSRG uses the Berggren basis to include effects from continuum coupling and describes the resonance and non-resonant continuum properties of weakly bound and unbound nuclei.

There are still many challenges on the path to developing IMSRG. The IMSRG(2) approximation is computationally efficient and capable of accurately capturing dynamic correlations. However, when treating observables characterized by strong static or collective correlations, such as $E2$ transition probabilities, IMSRG(2) usually fails to precisely reproduce experimental values. This is typically attributed to the lack of contributions from many-particle many-hole excitations [256] and the large uncertainty of the nuclear force [165]. IMSRG(3) was developed by [257]; however, its computational demands are so immense that it cannot be applied to medium- and heavy-mass nuclei. Several new approximations have been proposed that aim to capture as many of the essential IMSRG(3) correlations as possible while minimizing the computational cost [258, 259] and it is still an open problem. G-IMSRG is a powerful tool to treat weakly bound and unbound nuclei but is currently limited to closed-shell nuclei. New methods that combine G-IMSRG and VS-IMSRG are on the way to broaden the applicability of G-IMSRG to open-shell nuclei.

Notably, methods such as GSM-CC and GCC are dedicated to providing a unified description of the structure, decay, and reactions within open quantum systems. These developments enable a meticulous study of exotic decays in the dripline region. Deformation and continuum effects have been demonstrated to significantly influence the $2p$ decay process. Additionally, the observed nucleon–nucleon correlations serve as a valuable tool for probing the internal structure of dripline nuclei. These studies enhance our understanding of the complex dynamics and universal properties within open quantum systems.

Meanwhile, the existing framework of GCC remains incomplete at a microscopic level; the description of the core wave function is relatively simplistic, capturing only the collective motions. Thus, advancements toward a more detailed, microscopic framework are anticipated in future developments. Another avenue can involve extending the model to multi-particle decay studies near or beyond the dripline, which have garnered significant interest recently. Their applications to reaction-related problems, such as analyzing cross sections and reaction mechanisms, would be invaluable in providing structural and reactive insights in both theoretical and experimental studies.

Acknowledgements We acknowledge the High-Performance Computing Platform of Peking University for providing the computational resources.

References

1. E. Epelbaum, H.W. Hammer, U.G. Meißner, Modern theory of nuclear forces. Rev. Mod. Phys. **81**, 1773–1825 (2009). https://doi.org/10.1103/RevModPhys.81.1773
2. R. Machleidt, D. Entem, Chiral effective field theory and nuclear forces. Phys. Rep. **503**, 1–75 (2011). https://doi.org/10.1016/j.physrep.2011.02.001
3. S. Binder, J. Langhammer, A. Calci et al., Ab initio path to heavy nuclei. Phys. Lett. B **736**, 119–123 (2014). https://doi.org/10.1016/j.physletb.2014.07.010
4. G. Hagen, A. Ekström, C. Forssén et al., Neutron and weak-charge distributions of the ^{48}Ca nucleus. Nat. Phys. **12**, 186 (2016). https://doi.org/10.1038/nphys3529
5. G. Hagen, G.R. Jansen, T. Papenbrock, Structure of ^{78}Ni from first-principles computations. Phys. Rev. Lett. **117**, 172501 (2016). https://doi.org/10.1103/PhysRevLett.117.172501
6. B.S. Hu, F.R. Xu, Z.H. Sun et al., Ab initio nuclear many-body perturbation calculations in the Hartree-Fock basis. Phys. Rev. C **94**, 014303 (2016). https://doi.org/10.1103/PhysRevC.94.014303
7. T.D. Morris, J. Simonis, S.R. Stroberg et al., Structure of the lightest tin isotopes. Phys. Rev. Lett. **120**, 152503 (2018). https://doi.org/10.1103/PhysRevLett.120.152503
8. P. Gysbers, G. Hagen, J.D. Holt et al., Discrepancy between experimental and theoretical β-decay rates resolved from first principles. Nat. Phys. **15**, 428–431 (2019). https://doi.org/10.1038/s41567-019-0450-7
9. B.N. Lu, N. Li, S. Elhatisari et al., Perturbative quantum monte Carlo method for nuclear physics. Phys. Rev. Lett. **128**, 242501 (2022). https://doi.org/10.1103/PhysRevLett.128.242501
10. B.S. Hu, W.G. Jiang, T. Miyagi et al., Ab initio predictions link the neutron skin of ^{208}Pb to nuclear forces. Nat. Phys. **18**, 1196 (2022). https://doi.org/10.1038/s41567-022-01715-8
11. S. Weinberg, Nuclear forces from chiral Lagrangians. Phys. Lett. B **251**, 288–292 (1990). https://doi.org/10.1016/0370-2693(90)90938-3
12. S. Weinberg, Effective chiral Lagrangians for nucleon-pion interactions and nuclear forces. Nucl. Phys. B **363**, 3–18 (1991). https://doi.org/10.1016/0550-3213(91)90231-L
13. C. Ordóñez, U. van Kolck, Chiral Lagrangians and nuclear forces. Phys. Lett. B **291**, 459–464 (1992). https://doi.org/10.1016/0370-2693(92)91404-W
14. P. Navrátil, V.G. Gueorguiev, J.P. Vary et al., Structure of A=10-13 nuclei with two- plus three-nucleon interactions from chiral effective field theory. Phys. Rev. Lett. **99**, 042501 (2007). https://doi.org/10.1103/PhysRevLett.99.042501
15. T. Otsuka, T. Suzuki, J.D. Holt et al., Three-body forces and the limit of oxygen isotopes. Phys. Rev. Lett. **105**, 032501 (2010). https://doi.org/10.1103/PhysRevLett.105.032501
16. R. Roth, J. Langhammer, A. Calci et al., Similarity-transformed chiral NN+3N interactions for the ab initio description of ^{12}**C** and ^{16}**O**. Phys. Rev. Lett. **107**, 072501 (2011). https://doi.org/10.1103/PhysRevLett.107.072501
17. P. Maris, J.P. Vary, P. Navrátil et al., Origin of the anomalous long lifetime of ^{14}C. Phys. Rev. Lett. **106**, 202502 (2011). https://doi.org/10.1103/PhysRevLett.106.202502
18. G. Hagen, M. Hjorth-Jensen, G.R. Jansen et al., Continuum effects and three-nucleon forces in neutron-rich oxygen isotopes. Phys. Rev. Lett. **108**, 242501 (2012). https://doi.org/10.1103/PhysRevLett.108.242501
19. H. Hergert, S. Binder, A. Calci et al., Ab initio calculations of even oxygen isotopes with chiral two-plus-three-nucleon interactions. Phys. Rev. Lett. **110**, 242501 (2013). https://doi.org/10.1103/PhysRevLett.110.242501
20. J.D. Holt, J. Menéndez, A. Schwenk, Three-body forces and proton-rich nuclei. Phys. Rev. Lett. **110**, 022502 (2013). https://doi.org/10.1103/PhysRevLett.110.022502
21. S.K. Bogner, H. Hergert, J.D. Holt et al., Nonperturbative shell-model interactions from the in-medium similarity renormalization group. Phys. Rev. Lett. **113**, 142501 (2014). https://doi.org/10.1103/PhysRevLett.113.142501
22. T. Fukui, L. De Angelis, Y.Z. Ma et al., Realistic shell-model calculations for p-shell nuclei including contributions of

a chiral three-body force. Phys. Rev. C **98**, 044305 (2018). https://doi.org/10.1103/PhysRevC.98.044305

23. Y. Ma, F. Xu, L. Coraggio et al., Chiral three-nucleon force and continuum for dripline nuclei and beyond. Phys. Lett. B **802**, 135257 (2020). https://doi.org/10.1016/j.physletb.2020.135257
24. K. Hebeler, S.K. Bogner, R.J. Furnstahl et al., Improved nuclear matter calculations from chiral low-momentum interactions. Phys. Rev. C **83**, 031301(R) (2011). https://doi.org/10.1103/PhysRevC.83.031301
25. J. Simonis, S.R. Stroberg, K. Hebeler et al., Saturation with chiral interactions and consequences for finite nuclei. Phys. Rev. C **96**, 014303 (2017). https://doi.org/10.1103/PhysRevC.96.014303
26. W.G. Jiang, A. Ekström, C. Forssén et al., Accurate bulk properties of nuclei from A=2 to ∞ from potentials with Δ isobars. Phys. Rev. C **102**, 054301 (2020). https://doi.org/10.1103/PhysRevC.102.054301
27. V. Somà, P. Navrátil, F. Raimondi et al., Novel chiral Hamiltonian and observables in light and medium-mass nuclei. Phys. Rev. C **101**, 014318 (2020). https://doi.org/10.1103/PhysRevC.101.014318
28. S.R. Stroberg, J.D. Holt, A. Schwenk et al., Ab initio limits of atomic nuclei. Phys. Rev. Lett. **126**, 022501 (2021). https://doi.org/10.1103/PhysRevLett.126.022501
29. K. Hebeler, Three-nucleon forces: implementation and applications to atomic nuclei and dense matter. Phys. Rep. **890**, 1–116 (2021). https://doi.org/10.1016/j.physrep.2020.08.009
30. S. Zhang, Z. Cheng, J. Li et al., Ab initio Gamow shell model with chiral three-nucleon force for ^{14}O isotones. Chin. Sci. Bull. **67**, 4101–4107 (2022). https://doi.org/10.1360/TB-2022-0432
31. S. Bogner, R. Furnstahl, S. Ramanan et al., Low-momentum interactions with smooth cutoffs. Nucl. Phys. A **784**, 79–103 (2007). https://doi.org/10.1016/j.nuclphysa.2006.11.123
32. S. Bogner, R. Furnstahl, P. Maris et al., Convergence in the no-core shell model with low-momentum two-nucleon interactions. Nucl. Phys. A **801**, 21–42 (2008). https://doi.org/10.1016/j.nuclphysa.2007.12.008
33. E.D. Jurgenson, P. Navrátil, R.J. Furnstahl, Evolution of nuclear many-body forces with the similarity renormalization group. Phys. Rev. Lett. **103**, 082501 (2009). https://doi.org/10.1103/PhysRevLett.103.082501
34. S.D. Glazek, K.G. Wilson, Renormalization of Hamiltonians. Phys. Rev. D **48**, 5863–5872 (1993). https://doi.org/10.1103/PhysRevD.48.5863
35. F. Wegner, Flow-equations for Hamiltonians. Ann. der Phys. **506**, 77 (1994). https://doi.org/10.1002/andp.19945060203
36. K. Tsukiyama, S.K. Bogner, A. Schwenk, In-medium similarity renormalization group for nuclei. Phys. Rev. Lett. **106**, 222502 (2011). https://doi.org/10.1103/PhysRevLett.106.222502
37. H. Hergert, S. Bogner, T. Morris et al., The in-medium similarity renormalization group: a novel ab initio method for nuclei. Phys. Rep. **621**, 165–222 (2016). https://doi.org/10.1016/j.physrep.2015.12.007
38. S.R. Stroberg, H. Hergert, S.K. Bogner et al., Nonempirical interactions for the nuclear shell model: an update. Annu. Rev. Nucl. Part. Sci. **69**, 307–362 (2019). https://doi.org/10.1146/annurev-nucl-101917-021120
39. K. Tsukiyama, S.K. Bogner, A. Schwenk, In-medium similarity renormalization group for open-shell nuclei. Phys. Rev. C **85**, 061304(R) (2012). https://doi.org/10.1103/PhysRevC.85.061304
40. S.R. Stroberg, A. Calci, H. Hergert et al., Nucleus-dependent valence-space approach to nuclear structure. Phys. Rev. Lett. **118**, 032502 (2017). https://doi.org/10.1103/PhysRevLett.118.032502
41. G. Hagen, T. Papenbrock, D.J. Dean et al., Ab initio coupled-cluster approach to nuclear structure with modern nucleon-nucleon interactions. Phys. Rev. C **82**, 034330 (2010). https://doi.org/10.1103/PhysRevC.82.034330
42. G. Hagen, T. Papenbrock, M. Hjorth-Jensen et al., Coupled-cluster computations of atomic nuclei. Rep. Prog. Phys. **77**, 096302 (2014). https://doi.org/10.1088/0034-4885/77/9/096302
43. S. Novario, P. Gysbers, J. Engel et al., Coupled-cluster calculations of neutrinoless double-β decay in ^{48}Ca. Phys. Rev. Lett. **126**, 182502 (2021). https://doi.org/10.1103/PhysRevLett.126.182502
44. J.D. Holt, J. Menéndez, J. Simonis et al., Three-nucleon forces and spectroscopy of neutron-rich calcium isotopes. Phys. Rev. C **90**, 024312 (2014). https://doi.org/10.1103/PhysRevC.90.024312
45. A. Tichai, J. Langhammer, S. Binder et al., Hartree–Fock many-body perturbation theory for nuclear ground-states. Phys. Lett. B **756**, 283–288 (2016). https://doi.org/10.1016/j.physletb.2016.03.029
46. W.H. Dickhoff, C. Barbieri, Self-consistent Green's function method for nuclei and nuclear matter. Prog. Part. Nucl. Phys. **52**, 377–496 (2004). https://doi.org/10.1016/j.ppnp.2004.02.038
47. T. Miyagi, S.R. Stroberg, P. Navrátil et al., Converged ab initio calculations of heavy nuclei. Phys. Rev. C **105**, 014302 (2022). https://doi.org/10.1103/PhysRevC.105.014302
48. A. Tichai, P. Arthuis, H. Hergert et al., Adg: automated generation and evaluation of many-body diagrams. Eur. Phys. J. A **58**, 2 (2022). https://doi.org/10.1140/epja/s10050-021-00621-6
49. H. Hergert, S. Binder, A. Calci et al., Ab initio calculations of even oxygen isotopes with chiral two-plus-three-nucleon interactions. Phys. Rev. Lett. **110**, 242501 (2013). https://doi.org/10.1103/PhysRevLett.110.242501
50. H. Hergert, S.K. Bogner, T.D. Morris et al., Ab initio multireference in-medium similarity renormalization group calculations of even calcium and nickel isotopes. Phys. Rev. C **90**, 041302 (2014). https://doi.org/10.1103/PhysRevC.90.041302
51. T. Duguet, Symmetry broken and restored coupled-cluster theory: I. Rotational symmetry and angular momentum. J. Phys. G **42**, 025107 (2014). https://doi.org/10.1088/0954-3899/42/2/025107
52. J.M. Yao, B. Bally, J. Engel et al., Ab initio treatment of collective correlations and the neutrinoless double beta decay of ^{48}Ca. Phys. Rev. Lett. **124**, 232501 (2020). https://doi.org/10.1103/PhysRevLett.124.232501
53. Q. Yuan, S.Q. Fan, B.S. Hu et al., Deformed in-medium similarity renormalization group. Phys. Rev. C **105**, L061303 (2022). https://doi.org/10.1103/PhysRevC.105.L061303
54. N. Michel, W. Nazarewicz, M. Płoszajczak et al., Shell model in the complex energy plane. J. Phys. G **36**, 013101 (2009). https://doi.org/10.1088/0954-3899/36/1/013101
55. T. Berggren, On the use of resonant states in eigenfunction expansions of scattering and reaction amplitudes. Nucl. Phys. A **109**, 265–287 (1968). https://doi.org/10.1016/0375-9474(68)90593-9
56. R. Liotta, E. Maglione, N. Sandulescu et al., A representation to describe nuclear processes in the continuum. Phys. Lett. B **367**, 1–4 (1996). https://doi.org/10.1016/0370-2693(95)01415-2
57. B.S. Hu, Q. Wu, Z.H. Sun et al., Ab initio gamow in-medium similarity renormalization group with resonance and continuum. Phys. Rev. C **99**, 061302(R) (2019). https://doi.org/10.1103/PhysRevC.99.061302
58. B. Acharya, C. Ji, D. Phillips, Implications of a matter-radius measurement for the structure of carbon-22. Phys. Lett. B **723**, 196–200 (2013). https://doi.org/10.1016/j.physletb.2013.04.055
59. T. Suzuki, T. Otsuka, C. Yuan et al., Two-neutron "halo" from the low-energy limit of neutron-neutron interaction: applications to drip-line nuclei ^{22}C and ^{24}O. Phys. Lett. B **753**, 199–203 (2016). https://doi.org/10.1016/j.physletb.2015.12.001

60. X.X. Sun, J. Zhao, S.G. Zhou, Shrunk halo and quenched shell gap at N=16 in ^{22}C: inversion of sd states and deformation effects. Phys. Lett. B **785**, 530–535 (2018). https://doi.org/10.1016/j.physletb.2018.08.071
61. S. Elhatisari, D. Lee, G. Rupak et al., *Ab initio* alpha-alpha scattering. Nature **528**, 111–114 (2015). https://doi.org/10.1038/nature16067
62. P. Navrátil, S. Quaglioni, G. Hupin et al., Unified *ab initio* approaches to nuclear structure and reactions. Phys. Scripta **91**, 053002 (2016). https://doi.org/10.1088/0031-8949/91/5/053002
63. A. Kumar, R. Kanungo, A. Calci et al., Nuclear force imprints revealed on the elastic scattering of protons with ^{10}C. Phys. Rev. Lett. **118**, 262502 (2017). https://doi.org/10.1103/PhysRevLett.118.262502
64. S. Quaglioni, C. Romero-Redondo, P. Navrátil, Three-cluster dynamics within an ab initio framework. Phys. Rev. C **88**, 034320 (2013). https://doi.org/10.1103/PhysRevC.88.034320
65. S. Quaglioni, C. Romero-Redondo, P. Navrátil, Erratum: Three-cluster dynamics within an ab initio framework [phys. rev. c 88, 034320 (2013)]. Phys. Rev. C **94**, 019902 (2016). https://doi.org/10.1103/PhysRevC.94.019902
66. N. Michel, M. Płoszajczak, *Gamow Shell Model, The Unified Theory of Nuclear Structure and Reactions*, Lecture Notes in Physics, vol. 983. (Springer, Cham, 2021). https://doi.org/10.1007/978-3-030-69356-5
67. S.M. Wang, N. Michel, W. Nazarewicz et al., Structure and decays of nuclear three-body systems: The Gamow coupled-channel method in Jacobi coordinates. Phys. Rev. C **96**, 044307 (2017). https://doi.org/10.1103/PhysRevC.96.044307
68. S.M. Wang, W. Nazarewicz, Puzzling two-proton decay of ^{67}Kr. Phys. Rev. Lett. **120**, 212502 (2018). https://doi.org/10.1103/PhysRevLett.120.212502
69. N. Michel, W. Nazarewicz, M. Płoszajczak, Description of the proton-decaying 0_2^+ resonance of the α particle. Phys. Rev. Lett. **131**, 242502 (2023). https://doi.org/10.1103/PhysRevLett.131.242502
70. S.M. Wang, W. Nazarewicz, Fermion pair dynamics in open quantum systems. Phys. Rev. Lett. **126**, 142501 (2021). https://doi.org/10.1103/PhysRevLett.126.142501
71. S.M. Wang, W. Nazarewicz, R.J. Charity et al., Nucleon-nucleon correlations in the extreme oxygen isotopes. J. Phys. G **49**, 10LT02 (2022). https://doi.org/10.1088/1361-6471/ac888f
72. S. Bogner, R. Furnstahl, A. Schwenk, From low-momentum interactions to nuclear structure. Prog. Part. Nucl. Phys. **65**, 94–147 (2010). https://doi.org/10.1016/j.ppnp.2010.03.001
73. S.K. Bogner, R.J. Furnstahl, R.J. Perry, Similarity renormalization group for nucleon-nucleon interactions. Phys. Rev. C **75**, 061001(R) (2007). https://doi.org/10.1103/PhysRevC.75.061001
74. K. Hebeler, Momentum-space evolution of chiral three-nucleon forces. Phys. Rev. C **85**, 021002 (2012). https://doi.org/10.1103/PhysRevC.85.021002
75. R. Roth, S. Binder, K. Vobig et al., Medium-mass nuclei with normal-ordered chiral NN+3N interactions. Phys. Rev. Lett. **109**, 052501 (2012). https://doi.org/10.1103/PhysRevLett.109.052501
76. W. Magnus, On the exponential solution of differential equations for a linear operator. Pure Appl. Math **7**, 649–673 (1954). https://doi.org/10.1002/cpa.3160070404
77. T.D. Morris, N.M. Parzuchowski, S.K. Bogner, Magnus expansion and in-medium similarity renormalization group. Phys. Rev. C **92**, 034331 (2015). https://doi.org/10.1103/PhysRevC.92.034331
78. Y. Sun, P.M. Walker, F.R. Xu et al., Rotation-driven prolate-to-oblate shape phase transition in 190W: a projected shell model study. Phys. Lett. B **659**, 165–169 (2008). https://doi.org/10.1016/j.physletb.2007.10.067
79. H.L. Liu, F.R. Xu, P.M. Walker et al., Effects of high-order deformation on high-k isomers in superheavy nuclei. Phys. Rev. C **83**, 011303 (2011). https://doi.org/10.1103/PhysRevC.83.011303
80. T. Dytrych, K.D. Launey, J.P. Draayer et al., Collective modes in light nuclei from first principles. Phys. Rev. Lett. **111**, 252501 (2013). https://doi.org/10.1103/PhysRevLett.111.252501
81. T. Dytrych, K.D. Launey, J.P. Draayer et al., Physics of nuclei: key role of an emergent symmetry. Phys. Rev. Lett. **124**, 042501 (2020). https://doi.org/10.1103/PhysRevLett.124.042501
82. S.J. Novario, G. Hagen, G.R. Jansen et al., Charge radii of exotic neon and magnesium isotopes. Phys. Rev. C **102**, 051303 (2020). https://doi.org/10.1103/PhysRevC.102.051303
83. G. Hagen, S.J. Novario, Z.H. Sun et al., Angular-momentum projection in coupled-cluster theory: structure of ^{34}Mg. Phys. Rev. C **105**, 064311 (2022). https://doi.org/10.1103/PhysRevC.105.064311
84. R. Roth, P. Navrátil, Ab initio study of ^{40}Ca with an importance-truncated no-core shell model. Phys. Rev. Lett. **99**, 092501 (2007). https://doi.org/10.1103/PhysRevLett.99.092501
85. R. Roth, Importance truncation for large-scale configuration interaction approaches. Phys. Rev. C **79**, 064324 (2009). https://doi.org/10.1103/PhysRevC.79.064324
86. M.A. Caprio, P. Maris, J.P. Vary et al., Collective rotation from ab initio theory. Int. J. Mod. Phys. E **24**, 1541002 (2015). https://doi.org/10.1142/s0218301315410025
87. T. Abe, P. Maris, T. Otsuka et al., Ground-state properties of light 4n self-conjugate nuclei in ab initio no-core monte Carlo shell model calculations with nonlocal NN interactions. Phys. Rev. C **104**, 054315 (2021). https://doi.org/10.1103/PhysRevC.104.054315
88. M.G. Mayer, J.H.D. Jensen, *Elementary Theory of Nuclear Shell Structure* (Wiley, New York, 1955)
89. B.A. Brown, B.H. Wildenthal, Status of the nuclear shell model. Annu. Rev. Nucl. Part. Sci. **38**, 29–66 (1988). https://doi.org/10.1146/annurev.ns.38.120188.000333
90. T. Otsuka, M. Honma, T. Mizusaki et al., Monte Carlo shell model for atomic nuclei. Prog. Part. Nucl. Phys. **47**, 319–400 (2001). https://doi.org/10.1016/S0146-6410(01)00157-0
91. E. Caurier, G. Martínez-Pinedo, F. Nowacki et al., The shell model as a unified view of nuclear structure. Rev. Mod. Phys. **77**, 427–488 (2005). https://doi.org/10.1103/RevModPhys.77.427
92. B.A. Brown, The nuclear shell model towards the drip lines. Prog. Part. Nucl. Phys. **47**, 517–599 (2001). https://doi.org/10.1016/S0146-6410(01)00159-4
93. P. Navrátil, J.P. Vary, B.R. Barrett, Properties of ^{12}C in the ab initio nuclear shell model. Phys. Rev. Lett. **84**, 5728–5731 (2000). https://doi.org/10.1103/PhysRevLett.84.5728
94. P. Navrátil, J.P. Vary, B.R. Barrett, Large-basis ab initio no-core shell model and its application to ^{12}C. Phys. Rev. C **62**, 054311 (2000). https://doi.org/10.1103/PhysRevC.62.054311
95. N. Shimizu, T. Mizusaki, Y. Utsuno et al., Thick-restart block Lanczos method for large-scale shell-model calculations. Comput. Phys. Commun. **244**, 372–384 (2019). https://doi.org/10.1016/j.cpc.2019.06.011
96. J. Okołowicz, M. Płoszajczak, I. Rotter, Dynamics of quantum systems embedded in a continuum. Phys. Rep. **374**, 271–383 (2003). https://doi.org/10.1016/S0370-1573(02)00366-6
97. N. Michel, W. Nazarewicz, M. Płoszajczak et al., Shell model in the complex energy plane. J. Phys. G Nucl. Part. Phys. **36**, 013101 (2008). https://doi.org/10.1088/0954-3899/36/1/013101
98. I. Tanihata, H. Hamagaki, O. Hashimoto et al., Measurements of interaction cross sections and nuclear radii in the light p-shell region. Phys. Rev. Lett. **55**, 2676–2679 (1985). https://doi.org/10.1103/PhysRevLett.55.2676

99. A.S. Jensen, K. Riisager, D.V. Fedorov et al., Structure and reactions of quantum halos. Rev. Mod. Phys. **76**, 215–261 (2004). https://doi.org/10.1103/RevModPhys.76.215
100. R. Id Betan, R.J. Liotta, N. Sandulescu et al., Two-particle resonant states in a many-body mean field. Phys. Rev. Lett. **89**, 042501 (2002). https://doi.org/10.1103/PhysRevLett.89.042501
101. N. Michel, W. Nazarewicz, M. Płoszajczak et al., Gamow shell model description of neutron-rich nuclei. Phys. Rev. Lett. **89**, 042502 (2002). https://doi.org/10.1103/PhysRevLett.89.042502
102. R. Kanungo, A. Sanetullaev, J. Tanaka et al., Evidence of soft dipole resonance in ^{11}Li with isoscalar character. Phys. Rev. Lett. **114**, 192502 (2015). https://doi.org/10.1103/PhysRevLett.114.192502
103. K. Fossez, J. Rotureau, N. Michel et al., Single-particle and collective motion in unbound deformed ^{39}Mg. Phys. Rev. C **94**, 054302 (2016). https://doi.org/10.1103/PhysRevC.94.054302
104. G. Colò, A novel way to study the nuclear collective excitations. Nucl. Sci. Tech. **34**, 189 (2023). https://doi.org/10.1007/s41365-023-01343-8
105. Z. Sun, Q. Wu, Z. Zhao et al., Resonance and continuum gamow shell model with realistic nuclear forces. Phys. Lett. B **769**, 227–232 (2017). https://doi.org/10.1016/j.physletb.2017.03.054
106. J.G. Li, N. Michel, B.S. Hu et al., Ab initio no-core gamow shell-model calculations of multineutron systems. Phys. Rev. C **100**, 054313 (2019). https://doi.org/10.1103/PhysRevC.100.054313
107. B. Hu, Q. Wu, J. Li et al., An ab-initio gamow shell model approach with a core. Phys. Lett. B **802**, 135206 (2020). https://doi.org/10.1016/j.physletb.2020.135206
108. Y. Ma, F. Xu, N. Michel et al., Continuum and three-nucleon force in borromean system: The 17ne case. Phys. Lett. B **808**, 135673 (2020). https://doi.org/10.1016/j.physletb.2020.135673
109. J.G. Li, N. Michel, W. Zuo et al., Resonances of A=4 T=1 isospin triplet states within the ab initio no-core gamow shell model. Phys. Rev. C **104**, 024319 (2021). https://doi.org/10.1103/PhysRevC.104.024319
110. J.G. Li, N. Michel, W. Zuo et al., Unbound spectra of neutron-rich oxygen isotopes predicted by the gamow shell model. Phys. Rev. C **103**, 034305 (2021). https://doi.org/10.1103/PhysRevC.103.034305
111. Y.F. Geng, J.G. Li, Y.Z. Ma et al., Excitation spectra of the heaviest carbon isotopes investigated within the cd-Bonn Gamow shell model. Phys. Rev. C **106**, 024304 (2022). https://doi.org/10.1103/PhysRevC.106.024304
112. S. Zhang, Y. Ma, J. Li et al., The roles of three-nucleon force and continuum coupling in mirror symmetry breaking of oxygen mass region. Phys. Lett. B **827**, 136958 (2022). https://doi.org/10.1016/j.physletb.2022.136958
113. S. Zhang, F.R. Xu, J.G. Li et al., Ab initio descriptions of A=16 mirror nuclei with resonance and continuum coupling. Phys. Rev. C **108**, 064316 (2023). https://doi.org/10.1103/PhysRevC.108.064316
114. Z.C. Xu, S. Zhang, J.G. Li et al., Complex valence-space effective operators for observables: the Gamow-teller transition. Phys. Rev. C **108**, L031301 (2023). https://doi.org/10.1103/PhysRevC.108.L031301
115. S. Zhang, Y.F. Geng, F.R. Xu, Ab initio Gamow shell-model calculations for dripline nuclei. Nucl. Tech. **46**, 121–128 (2023). https://doi.org/10.11889/j.0253-3219.2023.hjs.46.080012
116. G. Hagen, D. Dean, M. Hjorth-Jensen et al., Complex coupled-cluster approach to an ab-initio description of open quantum systems. Phys. Lett. B **656**, 169–173 (2007). https://doi.org/10.1016/j.physletb.2007.07.072
117. S.M. Wang, W. Nazarewicz, Puzzling two-proton decay of ^{67}Kr. Phys. Rev. Lett. **120**, 212502 (2018). https://doi.org/10.1103/PhysRevLett.120.212502
118. G. Hagen, M. Hjorth-Jensen, N. Michel, Gamow shell model and realistic nucleon-nucleon interactions. Phys. Rev. C **73**, 064307 (2006). https://doi.org/10.1103/PhysRevC.73.064307
119. D.J. Rowe, Equations-of-motion method and the extended shell model. Rev. Mod. Phys. **40**, 153–166 (1968). https://doi.org/10.1103/RevModPhys.40.153
120. N.M. Parzuchowski, T.D. Morris, S.K. Bogner, Ab initio excited states from the in-medium similarity renormalization group. Phys. Rev. C **95**, 044304 (2017). https://doi.org/10.1103/PhysRevC.95.044304
121. M. Pfützner, I. Mukha, S.M. Wang, Two-proton emission and related phenomena. Prog. Part. Nucl. Phys. **123**, 104050 (2023). https://doi.org/10.1016/j.ppnp.2023.104050
122. L. Zhou, D.Q. Fang, S.M. Wang et al., Recent progress in two-proton radioactivity. Nucl. Sci. Tech. **33**, 105 (2022). https://doi.org/10.1007/s41365-022-01091-1
123. S. Saito, Interaction between clusters and Pauli principle. Prog. Theor. Phys. **41**, 705 (1969)
124. V. Kukulin, V. Pomerantsev, The orthogonal projection method in the scattering theory. Ann. Phys. (NY) **111**, 330 (1978)
125. P. Descouvemont, C. Daniel, D. Baye, Three-body systems with Lagrange-mesh techniques in hyperspherical coordinates. Phys. Rev. C **67**, 044309 (2003). https://doi.org/10.1103/PhysRevC.67.044309
126. I.J. Thompson, B.V. Danilin, V.D. Efros et al., Pauli blocking in three-body models of halo nuclei. Phys. Rev. C **61**, 024318 (2000). https://doi.org/10.1103/PhysRevC.61.024318
127. I.J. Thompson, F.M. Nunes, B.V. Danilin, FaCE: a tool for three body Faddeev calculations with core excitation. Comput. Phys. Commun. **161**, 87–107 (2004). https://doi.org/10.1016/j.cpc.2004.03.007
128. B. Gyarmati, T. Vertse, On the normalization of Gamow functions. Nucl. Phys. A **160**, 523–528 (1971). https://doi.org/10.1016/0375-9474(71)90095-9
129. N. Michel, W. Nazarewicz, M. Płoszajczak et al., Gamow shell model description of weakly bound nuclei and unbound nuclear states. Phys. Rev. C **67**, 054311 (2003). https://doi.org/10.1103/PhysRevC.67.054311
130. N. Michel, Numerical treatment of the long-range Coulomb potential with Berggren bases. Phys. Rev. C **83**, 034325 (2011). https://doi.org/10.1103/PhysRevC.83.034325
131. E.B. Huo, K.R. Li, X.Y. Qu et al., Continuum skyrme Hartree–Fock–Bogoliubov theory with green's function method for neutron-rich ca, ni, zr, and sn isotopes. Nucl. Sci. Tech. **34**, 105 (2023). https://doi.org/10.1007/s41365-023-01261-9
132. S.Z. Xu, S.S. Zhang, X.Q. Jiang et al., The complex momentum representation approach and its application to low-lying resonances in ^{17} O and ^{29,31} F. Nucl. Sci. Tech. **34**, 5 (2023). https://doi.org/10.1007/s41365-022-01159-y
133. T. Berggren, On the use of resonant states in eigenfunction expansions of scattering and reaction amplitudes. Nucl. Phys. A **109**, 265–287 (1968). https://doi.org/10.1016/0375-9474(68)90593-9
134. K. Hagino, N. Rowley, A. Kruppa, A program for coupled-channel calculations with all order couplings for heavy-ion fusion reactions. Comput. Phys. Commun. **123**, 143–152 (1999). https://doi.org/10.1016/S0010-4655(99)00243-X
135. K. Hagino, Role of dynamical particle-vibration coupling in reconciliation of the $d_{3/2}$ puzzle for spherical proton emitters. Phys. Rev. C **64**, 041304 (2001). https://doi.org/10.1103/PhysRevC.64.041304
136. B. Barmore, A.T. Kruppa, W. Nazarewicz et al., Theoretical description of deformed proton emitters: nonadiabatic coupled-channel method. Phys. Rev. C **62**, 054315 (2000). https://doi.org/10.1103/PhysRevC.62.054315

137. A.T. Kruppa, W. Nazarewicz, Gamow and *r*-matrix approach to proton emitting nuclei. Phys. Rev. C **69**, 054311 (2004). https://doi.org/10.1103/PhysRevC.69.054311
138. J. Humblet, L. Rosenfeld, Theory of nuclear reactions I. Resonant states and collision matrix. Nucl. Phys. **26**, 529 (1961)
139. L.V. Grigorenko, R.C. Johnson, I.G. Mukha et al., Theory of two-proton radioactivity with application to ^{19}Mg and ^{48}Ni. Phys. Rev. Lett. **85**, 22–25 (2000). https://doi.org/10.1103/PhysRevLett.85.22
140. L.V. Grigorenko, M.V. Zhukov, Two-proton radioactivity and three-body decay. iii. Integral formulas for decay widths in a simplified semianalytical approach. Phys. Rev. C **76**, 014008 (2007). https://doi.org/10.1103/PhysRevC.76.014008
141. L.V. Grigorenko, T.D. Wiser, K. Miernik et al., Complete correlation studies of two-proton decays: ^{6}Be and ^{45}Fe. Phys. Lett. B **677**, 30–35 (2009). https://doi.org/10.1016/j.physletb.2009.04.085
142. P. Descouvemont, E. Tursunov, D. Baye, Three-body continuum states on a Lagrange mesh. Nucl. Phys. A **765**, 370–389 (2006). https://doi.org/10.1016/j.nuclphysa.2005.11.010
143. V. Vasilevsky, A.V. Nesterov, F. Arickx et al., Algebraic model for scattering in three-*s*-cluster systems. i. Theoretical background. Phys. Rev. C **63**, 034606 (2001). https://doi.org/10.1103/PhysRevC.63.034606
144. H. Esbensen, C.N. Davids, Coupled-channels treatment of deformed proton emitters. Phys. Rev. C **63**, 014315 (2000). https://doi.org/10.1103/PhysRevC.63.014315
145. A. Volya, Computational approaches to many-body dynamics of unstable nuclear systems, in *Proceedings of the International Conference 'Nuclear Theory in the Supercomputing Era'*, Khabarovsk, Russia (2014). arXiv:1412.6335
146. M. Peshkin, A. Volya, V. Zelevinsky, Non-exponential and oscillatory decays in quantum mechanics. Europhys. Lett. **107**, 40001 (2014). https://doi.org/10.1209/0295-5075/107/40001
147. M. Bender, R. Bernard, G. Bertsch et al., Future of nuclear fission theory. J. Phys. G **47**, 113002 (2020). https://doi.org/10.1088/1361-6471/abab4f
148. C.A. Bertulani, M.S. Hussein, G. Verde, Blurred femtoscopy in two-proton decay. Phys. Lett. B **666**, 86–90 (2008). https://doi.org/10.1016/j.physletb.2008.06.062
149. T. Oishi, K. Hagino, H. Sagawa, Role of diproton correlation in two-proton-emission decay of the ^{6}Be nucleus. Phys. Rev. C **90**, 034303 (2014). https://doi.org/10.1103/PhysRevC.90.034303
150. T. Oishi, M. Kortelainen, A. Pastore, Dependence of two-proton radioactivity on nuclear pairing models. Phys. Rev. C **96**, 044327 (2017). https://doi.org/10.1103/PhysRevC.96.044327
151. A.I. Baz', Y.B. Zel'dovich, A.M. Perelomov, *Scattering, reactions and decay in nonrelativistic quantum mechanics* (Israel Program for Scientific Translation, Jerusalem, 1969)
152. T. Ikegami, S. Iwata, Spectral density calculation by using the Chebyshev expansion. J. Comput. Chem. **23**, 310–318 (2002). https://doi.org/10.1002/jcc.10010
153. A. Volya, Time-dependent approach to the continuum shell model. Phys. Rev. C **79**, 044308 (2009). https://doi.org/10.1103/PhysRevC.79.044308
154. Y.L. Loh, S.N. Taraskin, S.R. Elliott, Fast Chebyshev-polynomial method for simulating the time evolution of linear dynamical systems. Phys. Rev. E **63**, 056706 (2001). https://doi.org/10.1103/PhysRevE.63.056706
155. M. Wang, W. Huang, F. Kondev et al., The AME 2020 atomic mass evaluation (II). tables, graphs and references*. Chin. Phys. C **45**, 030003 (2021). https://doi.org/10.1088/1674-1137/abddaf
156. A. Ekström, G. Baardsen, C. Forssén et al., Optimized chiral nucleon-nucleon interaction at next-to-next-to-leading order. Phys. Rev. Lett. **110**, 192502 (2013). https://doi.org/10.1103/PhysRevLett.110.192502
157. R. Kanungo, W. Horiuchi, G. Hagen et al., Proton distribution radii of $^{12-19}$C illuminate features of neutron halos. Phys. Rev. Lett. **117**, 102501 (2016). https://doi.org/10.1103/PhysRevLett.117.102501
158. J. Henderson, G. Hackman, P. Ruotsalainen et al., Testing microscopically derived descriptions of nuclear collectivity: Coulomb excitation of ^{22}Mg. Phys. Lett. B **782**, 468–473 (2018). https://doi.org/10.1016/j.physletb.2018.05.064
159. J. Henderson, G. Hackman, P. Ruotsalainen et al., Coulomb excitation of the $|T_z| = \frac{1}{2}$, A=23 mirror pair. Phys. Rev. C **105**, 034332 (2022). https://doi.org/10.1103/PhysRevC.105.034332
160. G. Hagen, M. Hjorth-Jensen, G.R. Jansen et al., Emergent properties of nuclei from ab initio coupled-cluster calculations*. Phys. Scr. **91**, 063006 (2016). https://doi.org/10.1088/0031-8949/91/6/063006
161. A. Poves, J. Retamosa, The onset of deformation at the N = 20 neutron shell closure far from stability. Phys. Lett. B **184**, 311–315 (1987). https://doi.org/10.1016/0370-2693(87)90171-7
162. E.K. Warburton, J.A. Becker, B.A. Brown, Mass systematics for A=29-44 nuclei: the deformed $A \sim 32$ region. Phys. Rev. C **41**, 1147–1166 (1990). https://doi.org/10.1103/PhysRevC.41.1147
163. T. Miyagi, S.R. Stroberg, J.D. Holt et al., Ab initio multishell valence-space Hamiltonians and the island of inversion. Phys. Rev. C **102**, 034320 (2020). https://doi.org/10.1103/PhysRevC.102.034320
164. A. Krieger, W. Nörtershäuser, C. Geppert et al., Frequency-comb referenced collinear laser spectroscopy of Be$^+$ for nuclear structure investigations and many-body qed tests. Appl. Phys. B **123**, 15 (2016). https://doi.org/10.1007/s00340-016-6579-5
165. V. Lapoux, V. Somà, C. Barbieri et al., Radii and binding energies in oxygen isotopes: a challenge for nuclear forces. Phys. Rev. Lett. **117**, 052501 (2016). https://doi.org/10.1103/PhysRevLett.117.052501
166. B. Ohayon, H. Rahangdale, A.J. Geddes et al., Isotope shifts in ^{20,22}Ne: precision measurements and global analysis in the framework of intermediate coupling. Phys. Rev. A **99**, 042503 (2019). https://doi.org/10.1103/PhysRevA.99.042503
167. D.T. Yordanov, M.L. Bissell, K. Blaum et al., Nuclear charge radii of $^{21-32}$Mg. Phys. Rev. Lett. **108**, 042504 (2012). https://doi.org/10.1103/PhysRevLett.108.042504
168. J. Hoppe, C. Drischler, K. Hebeler et al., Probing chiral interactions up to next-to-next-to-next-to-leading order in medium-mass nuclei. Phys. Rev. C **100**, 024318 (2019). https://doi.org/10.1103/PhysRevC.100.024318
169. M. Wang, Y.H. Zhang, X. Zhou et al., Mass measurement of upper *fp*-shell $N = Z - 2$ and $N = Z - 1$ nuclei and the importance of three-nucleon force along the $N = Z$ line. Phys. Rev. Lett. **130**, 192501 (2023). https://doi.org/10.1103/PhysRevLett.130.192501
170. K. Blaum, High-accuracy mass spectrometry with stored ions. Phys. Rep. **425**, 1–78 (2006). https://doi.org/10.1016/j.physrep.2005.10.011
171. T. Yamaguchi, H. Koura, Y. Litvinov et al., Masses of exotic nuclei. Prog. Part. Nucl. Phys. **120**, 103882 (2021). https://doi.org/10.1016/j.ppnp.2021.103882
172. J.Y. Zhang, R. Casten, D. Brenner, Empirical proton-neutron interaction energies. Linearity and saturation phenomena. Phys. Lett. B **227**, 1–5 (1989). https://doi.org/10.1016/0370-2693(89)91273-2
173. D. Brenner, C. Wesselborg, R. Casten et al., Empirical p-n interactions: global trends, configuration sensitivity and N=Z enhancements. Phys. Lett. B **243**, 1–6 (1990). https://doi.org/10.1016/0370-2693(90)90945-3

174. P. Van Isacker, D.D. Warner, D.S. Brenner, Test of Wigner's spin-isospin symmetry from double binding energy differences. Phys. Rev. Lett. **74**, 4607–4610 (1995). https://doi.org/10.1103/PhysRevLett.74.4607
175. C.X. Yuan, C. Qi, F.R. Xu et al., Mirror energy difference and the structure of loosely bound proton-rich nuclei around A=20. Phys. Rev. C **89**, 044327 (2014). https://doi.org/10.1103/PhysRevC.89.044327
176. P. Schury, C. Bachelet, M. Block et al., Precision mass measurements of rare isotopes near N=Z=33 produced by fast beam fragmentation. Phys. Rev. C **75**, 055801 (2007). https://doi.org/10.1103/PhysRevC.75.055801
177. I. Mardor, S.A.S. Andrés, T. Dickel et al., Mass measurements of as, se, and br nuclei, and their implication on the proton-neutron interaction strength toward the $N = Z$ line. Phys. Rev. C **103**, 034319 (2021). https://doi.org/10.1103/PhysRevC.103.034319
178. D.S. Brenner, R.B. Cakirli, R.F. Casten, Valence proton-neutron interactions throughout the mass surface. Phys. Rev. C **73**, 034315 (2006). https://doi.org/10.1103/PhysRevC.73.034315
179. J. Simonis, S.R. Stroberg, K. Hebeler et al., Saturation with chiral interactions and consequences for finite nuclei. Phys. Rev. C **96**, 014303 (2017). https://doi.org/10.1103/PhysRevC.96.014303
180. A.T. Gallant, J.C. Bale, T. Brunner et al., New precision mass measurements of neutron-rich calcium and potassium isotopes and three-nucleon forces. Phys. Rev. Lett. **109**, 032506 (2012). https://doi.org/10.1103/PhysRevLett.109.032506
181. K. Tanaka, T. Yamaguchi, T. Suzuki et al., Observation of a large reaction cross section in the drip-line nucleus ^{22}**C**. Phys. Rev. Lett. **104**, 062701 (2010). https://doi.org/10.1103/PhysRevLett.104.062701
182. N. Kobayashi, T. Nakamura, J.A. Tostevin et al., One- and two-neutron removal reactions from the most neutron-rich carbon isotopes. Phys. Rev. C **86**, 054604 (2012). https://doi.org/10.1103/PhysRevC.86.054604
183. L. Gaudefroy, W. Mittig, N.A. Orr et al., Direct mass measurements of ^{19}B, ^{22}C, ^{29}F, ^{31}Ne, ^{34}Na and other light exotic nuclei. Phys. Rev. Lett. **109**, 202503 (2012). https://doi.org/10.1103/PhysRevLett.109.202503
184. Y. Togano, T. Nakamura, Y. Kondo et al., Interaction cross section study of the two-neutron halo nucleus ^{22}C. Phys. Lett. B **761**, 412–418 (2016). https://doi.org/10.1016/j.physletb.2016.08.062
185. T. Heng, J.P. Vary, P. Maris, Ab initio no-core properties of ^{7}Li and ^{7}Be with the jisp16 and chiral NNLO$_{\text{opt}}$ interactions. Phys. Rev. C **95**, 014306 (2017). https://doi.org/10.1103/PhysRevC.95.014306
186. A. Ekström, G.R. Jansen, K.A. Wendt et al., Accurate nuclear radii and binding energies from a chiral interaction. Phys. Rev. C **91**, 051301 (2015). https://doi.org/10.1103/PhysRevC.91.051301
187. G. Hagen, T. Papenbrock, D.J. Dean, Solution of the center-of-mass problem in nuclear structure calculations. Phys. Rev. Lett. **103**, 062503 (2009). https://doi.org/10.1103/PhysRevLett.103.062503
188. C. Hoffman, T. Baumann, D. Bazin et al., Evidence for a doubly magic ^{24}O. Phys. Lett. B **672**, 17–21 (2009). https://doi.org/10.1016/j.physletb.2008.12.066
189. C.R. Hoffman, T. Baumann, J. Brown et al., Observation of a two-neutron cascade from a resonance in ^{24}O. Phys. Rev. C **83**, 031303 (2011). https://doi.org/10.1103/PhysRevC.83.031303
190. T. Nagahisa, W. Horiuchi, Examination of the ^{22}C radius determination with interaction cross sections. Phys. Rev. C **97**, 054614 (2018). https://doi.org/10.1103/PhysRevC.97.054614
191. L. Coraggio, A. Covello, A. Gargano et al., Shell-model calculations for neutron-rich carbon isotopes with a chiral nucleon-nucleon potential. Phys. Rev. C **81**, 064303 (2010). https://doi.org/10.1103/PhysRevC.81.064303
192. G.R. Jansen, J. Engel, G. Hagen et al., Ab initio coupled-cluster effective interactions for the shell model: application to neutron-rich oxygen and carbon isotopes. Phys. Rev. Lett. **113**, 142502 (2014). https://doi.org/10.1103/PhysRevLett.113.142502
193. Y.F. Gao, B.S. Cai, C.X. Yuan, Investigation of β^--decay half-life and delayed neutron emission with uncertainty analysis. Nucl. Sci. Tech. **34**, 9 (2023). https://doi.org/10.1007/s41365-022-01153-4
194. J.Z. Han, S. Xu, A. Jalili et al., Investigation of the level spectra of nuclei in the northeast region of doubly magic ^{40}Ca with intruder orbit $g_{9/2}$. Nucl. Sci. Tech. **34**, 85 (2023). https://doi.org/10.1007/s41365-023-01243-x
195. A.T. Kruppa, B. Barmore, W. Nazarewicz et al., Fine structure in the decay of deformed proton emitters: nonadiabatic approach. Phys. Rev. Lett. **84**, 4549–4552 (2000). https://doi.org/10.1103/PhysRevLett.84.4549
196. C.N. Davids, H. Esbensen, Particle-vibration coupling in proton decay of near-spherical nuclei. Phys. Rev. C **64**, 034317 (2001). https://doi.org/10.1103/PhysRevC.64.034317
197. C.N. Davids, H. Esbensen, Decay rate of triaxially deformed proton emitters. Phys. Rev. C **69**, 034314 (2004). https://doi.org/10.1103/PhysRevC.69.034314
198. G. Fiorin, E. Maglione, L.S. Ferreira, Theoretical description of deformed proton emitters: nonadiabatic quasiparticle method. Phys. Rev. C **67**, 054302 (2003). https://doi.org/10.1103/PhysRevC.67.054302
199. P. Arumugam, E. Maglione, L.S. Ferreira, Nonadiabatic quasiparticle description of triaxially deformed proton emitters. Phys. Rev. C **76**, 044311 (2007). https://doi.org/10.1103/PhysRevC.76.044311
200. L.V. Grigorenko, M.V. Zhukov, Two-proton radioactivity and three-body decay. II. Exploratory studies of lifetimes and correlations. Phys. Rev. C **68**, 054005 (2003). https://doi.org/10.1103/PhysRevC.68.054005
201. M. Gonçalves, N. Teruya, O. Tavares et al., Two-proton emission half-lives in the effective liquid drop model. Phys. Lett. B **774**, 14–19 (2017). https://doi.org/10.1016/j.physletb.2017.09.032
202. W. Nazarewicz, J. Dudek, R. Bengtsson et al., Microscopic study of the high-spin behaviour in selected A=80 nuclei. Nucl. Phys. A **435**, 397–447 (1985). https://doi.org/10.1016/0375-9474(85)90471-3
203. M. Yamagami, K. Matsuyanagi, M. Matsuo, Symmetry-unrestricted Skyrme–Hartree–Fock–Bogoliubov calculations for exotic shapes in N=Z nuclei from ^{64}Ge to ^{84}Mo. Nucl. Phys. A **693**, 579–602 (2001). https://doi.org/10.1016/S0375-9474(01)00918-6
204. K. Kaneko, M. Hasegawa, T. Mizusaki, Shape transition and oblate-prolate coexistence in $N = Z$ *fpg*-shell nuclei. Phys. Rev. C **70**, 051301 (2004). https://doi.org/10.1103/PhysRevC.70.051301
205. B. Pritychenko, M. Birch, B. Singh et al., Tables of $E2$ transition probabilities from the first 2^+ states in even-even nuclei. At. Data Nucl. Data Tables **107**, 1–139 (2016). https://doi.org/10.1016/j.adt.2015.10.001
206. Y. Aboussir, J. Pearson, A. Dutta et al., Nuclear mass formula via an approximation to the Hartree–Fock method. At. Data Nucl. Data Tables **61**, 127–176 (1995). https://doi.org/10.1016/S0092-640X(95)90014-4
207. Mass Explorer. http://massexplorer.frib.msu.edu/
208. P. Möller, A. Sierk, T. Ichikawa et al., Nuclear ground-state masses and deformations: FRDM (2012). At. Data Nucl. Data Tables **109–110**, 1–204 (2016). https://doi.org/10.1016/j.adt.2015.10.002

209. T. Goigoux, P. Ascher, B. Blank et al., Two-proton radioactivity of ^{67}Kr. Phys. Rev. Lett. **117**, 162501 (2016). https://doi.org/10.1103/PhysRevLett.117.162501
210. O.V. Bochkarev, L.V. Chulkov, A.A. Korsheninniicov et al., Democratic decay of ^{6}Be states. Nucl. Phys. A **505**, 215–240 (1989). https://doi.org/10.1016/0375-9474(89)90371-0
211. M. Pfützner, M. Karny, L.V. Grigorenko et al., Radioactive decays at limits of nuclear stability. Rev. Mod. Phys. **84**, 567–619 (2012). https://doi.org/10.1103/RevModPhys.84.567
212. P. Papka, R. Álvarez-Rodríguez, F. Nemulodi et al., Decay of ^{6}Be populated in the ^{6}Li (^{3}He,^{3} H) charge-exchange reaction. Phys. Rev. C **81**, 054308 (2010). https://doi.org/10.1103/PhysRevC.81.054308
213. F.C. Barker, *R*-matrix formulas for three-body decay widths. Phys. Rev. C **68**, 054602 (2003). https://doi.org/10.1103/PhysRevC.68.054602
214. B. Blank, M. Płoszajczak, Two-proton radioactivity. Rep. Prog. Phys. **71**, 046301 (2008). https://doi.org/10.1088/0034-4885/71/4/046301
215. R. Álvarez-Rodríguez, H.O.U. Fynbo, A.S. Jensen et al., Distinction between sequential and direct three-body decays. Phys. Rev. Lett. **100**, 192501 (2008). https://doi.org/10.1103/PhysRevLett.100.192501
216. L.V. Grigorenko, T.D. Wiser, K. Mercurio et al., Three-body decay of ^{6}Be. Phys. Rev. C **80**, 034602 (2009). https://doi.org/10.1103/PhysRevC.80.034602
217. I.A. Egorova, R.J. Charity, L.V. Grigorenko et al., Democratic decay of ^{6}Be exposed by correlations. Phys. Rev. Lett. **109**, 202502 (2012). https://doi.org/10.1103/PhysRevLett.109.202502
218. V. Chudoba, L.V. Grigorenko, A.S. Fomichev et al., Three-body correlations in direct reactions: Example of ^{6}Be populated in the (p, n) reaction. Phys. Rev. C **98**, 054612 (2018). https://doi.org/10.1103/PhysRevC.98.054612
219. D.X. Zhu, Y.Y. Xu, H.M. Liu et al., Two-proton radioactivity of the excited state within the Gamow-like and modified Gamow-like models. Nucl. Sci. Tech. **33**, 122 (2022). https://doi.org/10.1007/s41365-022-01116-9
220. S.M. Wang, W. Nazarewicz, R.J. Charity et al., Structure and decay of the extremely proton-rich nuclei ^{11,12}O. Phys. Rev. C **99**, 054302 (2019). https://doi.org/10.1103/PhysRevC.99.054302
221. D.R. Thompson, M. Lemere, Y.C. Tang, Systematic investigation of scattering problems with the resonating-group method. Nucl. Phys. A **286**, 53–66 (1977). https://doi.org/10.1016/0375-9474(77)90007-0
222. K. Miernik, W. Dominik, Z. Janas et al., Two-proton correlations in the decay of ^{45}Fe. Phys. Rev. Lett. **99**, 192501 (2007). https://doi.org/10.1103/PhysRevLett.99.192501
223. T.B. Webb, R.J. Charity, J.M. Elson et al., Particle decays of levels in ^{11,12}N and ^{12}O investigated with the invariant-mass method. Phys. Rev. C **100**, 024306 (2019). https://doi.org/10.1103/PhysRevC.100.024306
224. T.B. Webb, S.M. Wang, K.W. Brown et al., First observation of unbound ^{11}O, the mirror of the halo nucleus ^{11}Li. Phys. Rev. Lett. **122**, 122501 (2019). https://doi.org/10.1103/PhysRevLett.122.122501
225. L.V. Grigorenko, I.G. Mukha, I.J. Thompson et al., Two-proton widths of ^{12}O,^{16} Ne, and three-body mechanism of Thomas-Ehrman shift. Phys. Rev. Lett. **88**, 042502 (2002). https://doi.org/10.1103/PhysRevLett.88.042502
226. L.P. Kok, Accurate determination of the ground-state level of the ^{2}He nucleus. Phys. Rev. Lett. **45**, 427–430 (1980). https://doi.org/10.1103/PhysRevLett.45.427
227. T.B. Webb, R.J. Charity, J.M. Elson et al., Invariant-mass spectrum of ^{11}O. Phys. Rev. C **101**, 044317 (2020). https://doi.org/10.1103/PhysRevC.101.044317
228. H.T. Fortune, Energy and width of ^{11} O(g.s.). Phys. Rev. C **99**, 051302 (2019). https://doi.org/10.1103/PhysRevC.99.051302
229. E. Garrido, A.S. Jensen, Few-body structures in the mirror nuclei ^{11}O and ^{11}Li. Phys. Rev. C **101**, 034003 (2020). https://doi.org/10.1103/PhysRevC.101.034003
230. X. Mao, J. Rotureau, W. Nazarewicz et al., Gamow-shell-model description of Li isotopes and their mirror partners. Phys. Rev. C **102**, 024309 (2020). https://doi.org/10.1103/PhysRevC.102.024309
231. E. Merzbacher, *Quantum Mechanics* (Wiley, Hoboken, 1998)
232. E.J. Hellund, The decay of resonance radiation by spontaneous emission. Phys. Rev. **89**, 919–922 (1953). https://doi.org/10.1103/PhysRev.89.919
233. L.A. Khalfin, Contribution to the decay theory of a quasi-stationary state. Sov. Phys. JETP **6**, 1053 (1958)
234. M. Lévy, On the validity of the exponential law for the decay of an unstable particle. Il Nuovo Cimento **1955–1965**(14), 612–624 (1959). https://doi.org/10.1007/BF02726390
235. J. Schwinger, Field theory of unstable particles. Ann. Phys. **9**, 169–193 (1960). https://doi.org/10.1016/0003-4916(60)90027-0
236. R.G. Winter, Evolution of a quasi-stationary state. Phys. Rev. **123**, 1503–1507 (1961). https://doi.org/10.1103/PhysRev.123.1503
237. R.G. Newton, The exponential decay law of unstable systems. Ann. Phys. (N.Y.) **14**, 333–345 (1961). https://doi.org/10.1016/0003-4916(61)90060-4
238. M.L. Goldberger, K.M. Watson, Lifetime and decay of unstable particles in *S*-matrix theory. Phys. Rev. **136**, B1472–B1480 (1964). https://doi.org/10.1103/PhysRev.136.B1472
239. L. Fonda, G.C. Ghirardi, A. Rimini, Decay theory of unstable quantum systems. Rep. Prog. Phys. **41**, 587–631 (1978). https://doi.org/10.1088/0034-4885/41/4/003
240. P.T. Greenland, Seeking non-exponential decay. Nature **335**, 298–298 (1988). https://doi.org/10.1038/335298a0
241. G. Esposito, G. Marmo, G. Sudarshan, *From Classical to Quantum Mechanics: An Introduction to the Formalism, Foundations and Applications* (Cambridge University Press, Cambridge, 2004). https://doi.org/10.1017/CBO9780511610929
242. V. Fock, N. Krylov, On two main interpretations of energy-time uncertainty. J. Exp. Theor. Phys. **17**, 93 (1947)
243. M. Miyamoto, Zero energy resonance and the logarithmically slow decay of unstable multilevel systems. J. Math. Phys. **47**, 082103 (2006). https://doi.org/10.1063/1.2227260
244. D.F. Ramírez Jiménez, N.G. Kelkar, Quantum decay law: critical times and the equivalence of approaches. J. Phys. A **52**, 055201 (2019). https://doi.org/10.1088/1751-8121/aaf9f3
245. D.F. Ramírez Jiménez, N.G. Kelkar, Formal aspects of quantum decay. Phys. Rev. A **104**, 022214 (2021). https://doi.org/10.1103/PhysRevA.104.022214
246. S.M. Wang, W. Nazarewicz, A. Volya et al., Probing the non-exponential decay regime in open quantum systems. Phys. Rev. Res. **5**, 023183 (2023). https://doi.org/10.1103/PhysRevResearch.5.023183
247. C. Rothe, S.I. Hintschich, A.P. Monkman, Violation of the exponential-decay law at long times. Phys. Rev. Lett. **96**, 163601 (2006). https://doi.org/10.1103/PhysRevLett.96.163601
248. T. Mercouris, C.A. Nicolaides, Time dependence and properties of nonstationary states in the continuous spectrum of atoms. J. Phys. B **30**, 811 (1997). https://doi.org/10.1088/0953-4075/30/4/006

249. D.S. Onley, A. Kumar, Time dependence in quantum mechanics-study of a simple decaying system. Am. J. Phys. **60**, 432–439 (1992). https://doi.org/10.1119/1.16897
250. U. Peskin, H. Reisler, W.H. Miller, On the relation between unimolecular reaction rates and overlapping resonances. J. Chem. Phys. **101**, 9672–9680 (1994). https://doi.org/10.1063/1.467932
251. R. de la Madrid, Numerical calculation of the decay widths, the decay constants, and the decay energy spectra of the resonances of the delta-shell potential. Nucl. Phys. A **962**, 24–45 (2017). https://doi.org/10.1016/j.nuclphysa.2017.03.006
252. V.V. Sokolov, V.G. Zelevinsky, Dynamics and statistics of unstable quantum states. Nucl. Phys. A **504**, 562–588 (1989). https://doi.org/10.1016/0375-9474(89)90558-7
253. A. Volya, V. Zelevinsky, Non-hermitian effective Hamiltonian and continuum shell model. Phys. Rev. C **67**, 054322 (2003). https://doi.org/10.1103/PhysRevC.67.054322
254. A.I. Magunov, I. Rotter, S.I. Strakhova, Fano resonances in the overlapping regime. Phys. Rev. B **68**, 245305 (2003). https://doi.org/10.1103/PhysRevB.68.245305
255. K. Kravvaris, A. Volya, Quest for superradiance in atomic nuclei. AIP Conf. Proc. **1912**, 020010 (2017). https://doi.org/10.1063/1.5016135
256. S.R. Stroberg, J. Henderson, G. Hackman et al., Systematics of *e*2 strength in the *sd* shell with the valence-space in-medium similarity renormalization group. Phys. Rev. C **105**, 034333 (2022). https://doi.org/10.1103/PhysRevC.105.034333
257. M. Heinz, A. Tichai, J. Hoppe et al., In-medium similarity renormalization group with three-body operators. Phys. Rev. C **103**, 044318 (2021). https://doi.org/10.1103/PhysRevC.103.044318
258. B.C. He, S.R. Stroberg, Factorized approximation to the imsrg(3). (2024). arXiv:2405.19594
259. S.R. Stroberg, T.D. Morris, B.C. He, IMSRG with flowing 3 body operators, and approximations thereof (2024). arXiv:2406.13010